https://doi.org/10.5194/bg-2022-3
Preprint. Discussion started: 11 January 2022

Biogeosciences Discussions

Hydrodynamic and Biochemical Impacts on the Development of Hypoxia in the Louisiana–Texas Shelf Part I: Numerical Modeling and Hypoxia Mechanisms

Yanda Ou[1] and Z. George Xue[1,2,3]

[1]Department of Oceanography and Coastal Sciences, Louisiana State University, Baton Rouge, LA, 70803, USA.
[2]Center for Computation and Technology, Louisiana State University, Baton Rouge, LA, 70803, USA.
[3]Coastal Studies Institute, Louisiana State University, Baton Rouge, LA, 70803, USA

Correspondence to: Z. George Xue (zxue@lsu.edu)

Abstract. A three-dimensional coupled hydrodynamic–biogeochemical model with N, P, Si cycles and multiple phytoplankton and zooplankton functional groups was developed and applied to the Gulf of Mexico to study bottom dissolved oxygen dynamics. A 15-year hindcast was achieved covering the period of 2006-2020. Extensive model validation against in situ data demonstrates that the model is capable of reproducing vertical distributions of dissolved oxygen (DO), frequency distributions of hypoxia thickness, spatial distributions of bottom DO concentration and interannual variations of hypoxic area. The impacts of river plume and along-shore currents on bottom DO dynamics were examined based on multiyear bottom DO climatology, the corresponding long-term trends, and interannual variability. Model results suggest that mechanisms of bottom hypoxia developments are different between the west and east Louisiana–Texas Shelf waters. The mid-Atchafalaya nearshore (10–20 m) region firstly suffers from hypoxia in May, followed by the west-Mississippi nearshore region in June. Hypoxic waters expand in the following months and eventually merge in August. Sediment oxygen consumption (SOC) and water stratification (measured by potential energy anomaly, PEA) are two main factors modulating the variability of bottom DO concentration. Generalized Boosted Regression Models provide analysis of the relative importance of PEA and SOC. The analysis indicates that SOC is the main regulator in nearshore regions, and water stratification outcompetes the sedimentary biochemical processes in the offshore (20–50 m) regions. A strong quadratic relationship was found between hypoxic volume and hypoxic area, which suggests that the volume mostly results from the low DO in bottom water and can be potentially estimated based on the hypoxic area.

1 Introduction

The Louisiana–Texas (LaTex) Shelf in the northern Gulf of Mexico (nGoM) is one of the most notorious hypoxia affected areas in the world (bottom dissolved oxygen (DO) < 2 mg L^{-1}, Rabalais et al., 2002; Rabalais et al., 2007a; Justić and Wang, 2014). Regular mid-summer cruises since 1985 have shown that hypoxia usually first emerges in mid-May and persists through mid-September. The hypoxic water can cover as big as 23,000 km^2 and has a volume of up to 140 km^3 (Rabalais and Turner,

https://doi.org/10.5194/bg-2022-3
Preprint. Discussion started: 11 January 2022

2019; Rabalais and Baustian, 2020). Sensitivity experiments of hypoxia area reduction to different nutrient shrinking strategies by Fennel and Laurent (2018) suggested that to meet the hypoxic area reduction goal (reduce to < 5,000 km^2 in a 5-year running average) set by the Hypoxia Task Force (2008), a dual nutrient strategy with a reduction of 48 % of total nitrogen and inorganic phosphorus would be the most effective way. Although nitrogen is the ultimate limiting nutrient, phosphorus load reduction would also lead to a significant shrinkage of the hypoxia (Fennel and Laurent, 2018). Phosphorus limitation was deemed to be associated with the delayed onset of hypoxia and reduction of hypoxia area according to numerical studies (Laurent et al., 2012; Laurent and Fennel, 2014).

Coastal eutrophication in the LaTex Shelf was deemed to be important to a high rate of microbial respiration and depletion of DO (Conley et al., 2009; Rabalais et al., 2007b). Incubation studies in the LaTex Shelf suggested that SOC accounted for 20±4 % (Murrell and Lehrter, 2011) or 25±5.3 % (McCarthy et al., 2013) of below-pycnocline respiration, nearly 7-fold greater than the corresponding percentage at the water overlying sediments (3.7±0.8 %, McCarthy et al., 2013). The fraction of SOC over the total respiration rate at sediments and overlying water was ~87 % according to the measurements by McCarthy et al. (2013). As mentioned by Fennel et al. (2013), the corresponding SOC fraction reached 60 % when applying the water respiration rates of Murrell and Lehrter (2011) and sediment respiration rates of Rowe et al. (2002). Another numerical study (Yu et al., 2015) also pointed out that in the LaTex Shelf, oxygen consumption at the bottom water layer was more associated with SOC rather than water column respiration. While it is commonly accepted that bottom water oxygen concentration modulates SOC (e.g., Hetland and DiMarco, 2008; Murrell and Lehrter, 2011; Justić and Wang, 2014; Yu et al., 2015), McCarthy et al. (2013) argued that SOC was indeed driven by the abundance of organic matter in the sediment. It is SOC that determines bottom water oxygen concentration. An instantaneous remineralization parameterization built by Fennel et al. (2006, 2011) estimates SOC as a function of sediment detritus and phytoplankton only. Using this scheme, Große et al. (2019) found that the simulated SOC was supported by Mississippi nitrogen supply (51±9 %), Atchafalaya nitrogen supply (33±9 %), and open-boundary nitrogen supply (16±2 %). However, the instantaneous parameterization tends to underestimate SOC at the peak of blooms yet overestimate SOC once the blooms started. In a realistic environment, there should be a lag between the blooms and the peak SOC (Fennel et al., 2013). Recently, developments of coupled sediment–water models emphasize the importance of sedimentary biochemical processes on the SOC dynamics and evolution of bottom hypoxia in the shelf (Moriarty et al., 2018; Laurent et al., 2016). However, couple sediment–water models are computationally more expensive than simple parameterization of SOC. It is, therefore, crucial to balance the model efficiency and model complexity, especially for long-term hindcast.

Cruises data in the nGoM indicated that diatoms accounted for ~50 to ~65 % (inner-shelf) and ~48 to ~64 % (mid-shelf) of chlorophyll a in winter and spring, respectively, and ~30 % to ~46 % (inner-shelf) during summer and fall, respectively (Chakraborty and Lohrenz, 2015). A field survey documented the biovolume contribution of diatoms to the total phytoplankton could be as high as 80 % and 70 % during the upwelling seasons in 2013 and 2014, respectively (Anglès et al., 2019). In the

https://doi.org/10.5194/bg-2022-3
Preprint. Discussion started: 11 January 2022

Mississippi River plume, diatoms are the most diverse algal class accounting for over 42 % of all unique genotypes observed (Wawrik and Paul, 2004). The phytoplankton bloom in the shelf results from both cyanobacteria and diatoms (Wawrik and Paul, 2004; Schaeffer et al., 2012; Chakraborty et al., 2017). However, the phytoplankton community was highly simplified in previous numerical studies with only one phytoplankton functional group considered (e.g., Fennel et al., 2006, 2011, 2013; Laurent et al., 2012; Justić and Wang, 2014).

In addition to SOC and excess nutrient supply from the rivers, water column stratification also plays an important role in regulating the variability of bottom DO concentration in the LaTex Shelf. Stronger stratification prohibits ventilation of DO and thus results in less DO supply to the bottom water layer (Hetland and DiMarco, 2008; Bianchi et al., 2010; Fennel et al., 2011, 2013, 2016; Justić and Wang, 2014; Wang and Justić, 2009; Feng et al., 2014; Yu et al., 2015; Laurent et al., 2018). In the shelf, river freshwater plume supported by the Mississippi and the Atchafalaya Rivers would introduce buoyancy leading to a stable water column and weak DO ventilation processes (Mattern et al., 2013; Fennel and Testa, 2019). However, due to the different distances from major river mouths, the influence of freshwater-induced buoyancy would vary along the shelf. Moreover, the transports and deposition processes of organic matters would be affected by the coastal along-shore current systems resulting in different SOC gradients across the shelf. Although Hetland and DiMarco (2008) pointed out that in the west of Terrebonne Bay where stratification is usually weak, bottom hypoxia is controlled by bottom respiration, there is still a lack of discussions of dominated factors of bottom DO dynamics in different parts of the shelf.

In this study, we adapted and modified a coupled physical-biogeochemical model to the Gulf of Mexico. We introduced an oxygen and a phosphorus cycle to the North Pacific Ecosystem Model for Understanding Regional Oceanography (NEMURO, Kishi et al. 2007). The model has two phytoplankton and three zooplankton, functional groups, for a more comprehensive representation of the plankton community. An additional silicate limitation term is applied for the growth of the diatom functional group. We developed a simplified yet efficient SOC parameterization with two sedimentary organic pools to account for the time lags between bottom hypoxia peaks and bloom peaks. Based on a 15-year (2006–2020) hindcast, we aim to 1) understand the contributions of different factors in hypoxia evolution in different parts of the LaTex shelf; and 2) to provide daily hindcasts of physical and biochemical conditions to develop a hypoxia prediction model using machine learning techniques (see an accompanying paper in Part II). In the following sections, model description and modification, model set-ups, and data availability are given in Methods (Section 2), followed by extensive model validations from time series to spatial patterns and vertical structure (Section 3). The main findings of this study and discussion of the relative importance of different factors in modulating bottom DO variability are given in Section 4. Conclusions are addressed in the last section.

https://doi.org/10.5194/bg-2022-3
Preprint. Discussion started: 11 January 2022


Biogeosciences Discussions

2 Methods

2.1 Coupled hydrodynamic–biogeochemical model

We adapt the three-dimensional, free-surface, topography following numerical model, the Regional Ocean Model System (ROMS, version 3.7) on the platform of Coupled Ocean–Atmosphere–Wave–Sediment Transport modeling system (COAWST, Warner et al., 2010) to the GoM (Gulf–COAWST). ROMS solves finite difference approximations of Reynolds Averaged Navier–Stokes equations by applying hydrostatic and Boussinesq approximations with a split explicit time-stepping algorithm (Haidvogel et al., 2000; Shchepetkin and McWilliams, 2005, 2009). The biogeochemical model applied is largely based on the NEMURO developed by Kishi et al. (2007). NEMURO is a concentration-based, lower-trophic-level ecosystem model developed and parameterized for the North Pacific. The original NEMURO model has 11 concentration-based state variables including nitrate (NO_3), ammonium (NH_4), small and large phytoplankton biomass (SP and LP), small, large, and predatory zooplankton biomass (SZ, LZ, and PZ), particulate and dissolved organic nitrogen (PON and DON), particulate silica (Opal), and silicic acid ($Si(OH)_4$). NEMURO is known for its capability in distinguishing SZ, LZ, and PZ and provides a detailed analysis of the dynamics of different functional groups. It was widely used in studies of plankton biomass in regional scales (Fiechter and Moore 2009; Gomez et al., 2018; Shropshire et al., 2020). The embedded silicon cycle permits the inclusion of a diatom group (i.e., PL), which is deemed to be the dominant phytoplankton group in the nGoM.

2.2 Model modification

In a recent effort, Shropshire et al. (2020) adapted and modified NEMURO to the GoM with five structural changes as follows. (1) The grazing pathway of LZ on SP was removed since, in the GoM, the SP group is predominated by cyanobacteria and picoeukaryotes which are too small for direct feeding by most mesozooplankton (i.e., LP). (2) Linear function of mortality was applied for SP, LP, SZ, and LZ, while quadratic mortality was used for PZ accounting for predation pressure of unmodeled predators, like planktivorous fish. (3) The ammonium inhibition term in nitrate limitation function was no longer considered exponentially but followed the parameterization by Parker (1993). (4) Light limitation on photosynthesis was replaced with Platt et al.'s (1980) functional form which was also implemented in the newer version of NEMURO. (5) Constant C: Chl ratio was replaced with a variable C: Chl model according to the formulation by Li et al. (2010).

However, neither the modified (Shropshire et al., 2020) nor the original (Kishi et al., 2007) NEMURO model considered phosphorus and oxygen cycles. In this study, we introduced a phosphorus cycle into NEMURO, which includes three concentration-based state variables as phosphate (PO_4), particulate organic phosphorus (POP), and dissolved organic phosphorus (DOP). The phosphate limitation on phytoplankton growth was introduced using the Michaelis–Menten formula (Michaelis and Menten, 1913). In the NEMURO model, nitrogen serves as the common “currency”, while phosphorus and silicon are converted to nitrogen using the Redfield ratio of P: N: Si=1: 16: 16. In the river-dominated LaTex Shelf, inorganic and organic nutrients are mostly supplied by rivers. In our model, riverine DOP and POP were prescribed based on water

https://doi.org/10.5194/bg-2022-3
Preprint. Discussion started: 11 January 2022

quality measurements at river gages. When no measurement is available, the DOP and POP were approximated using dissolved organic nitrogen (DON) and particulate organic nitrogen (PON) measurements via the Redfield ratio of P: N=1: 16. We neglected the POP settling process but preserved these pools by introducing the stoichiometric ratio between phosphorus and nitrogen instead. In other words, the sinking process of POP was implicitly included by building linkages between PON and POP concentrations, as the sinking of PON was considered in the model. Governing equations for phosphorus state variables were given according to Equations 1–3. Please also refer to the appendices for more details of expressions of modified terms (Appendix A), state variables (Appendix Table B1), source and sink terms (Appendix Table B2), and values of parameters (Appendix Table B4).

$$\frac{d(PO_4)}{dt} = (ResPSn + ResPLn) \cdot RPO4N + (DecP2N + DecD2N) \cdot RPO4N + (ExcZSn + ExcZLn + ExcZPn) \cdot RPO4N - (GppPSn + GppPLn) \cdot RPO4N, \quad (1)$$

$$\frac{d(DOP)}{dt} = (DecP2D - DecD2N) \cdot RPO4N + (ExcPSn + ExcPLn) \cdot RPO4N, \quad (2)$$

$$\frac{d(POP)}{dt} = (MorPSn + MorPLn + MorZSn + MorZLn + MorZPn) \cdot RPO4N + (EgeZSn + EgeZLn + EgeZPn) \cdot RPO4N - (DecP2N + DecP2D) \cdot RPO4N, \quad (3)$$

We further adapted the oxygen cycle developed by Fennel et al. (2006, 2013) to NEMURO for hypoxia simulations. However, the biochemical dynamics of oxygen in our model are slightly different due to the different plankton functional groups considered. Biochemical sources for oxygen are contributed by photosynthesis of two phytoplankton functional groups, while the sinks are attributed to respirations of two phytoplankton functional groups, metabolism of three zooplankton functional groups, light-dependent nitrification (Olson, 1981; Fennel et al., 2006), aerobic decomposition of particulate and dissolved organic matter (measured as PON, and DON, respectively), and SOC. Wanninkhof's (1992) parameterization was implemented for estimates of oxygen air–sea flux. The biochemical dynamics of oxygen are adopted as follows (see detailed descriptions of variables and parameters in Appendix A–B):

$$\frac{d(Oxyg)}{dt} = (rOxNO_3 \cdot GppNPS + rOxNH_4 \cdot GppAPS) + (rOxNO_3 \cdot GppNPL + rOxNH_4 \cdot GppAPL) - ResPSn \cdot [RnewS \cdot rOxNO_3 + (1 - RnewS) \cdot rOxNH_4] - ResPLn \cdot [RnewL \cdot rOxNO_3 + (1 - RnewL) \cdot rOxNH_4] - rOxNH_4 \cdot (ExcZS + ExcZL + ExcZP)$$

https://doi.org/10.5194/bg-2022-3
Preprint. Discussion started: 11 January 2022


Biogeosciences Discussions Open Access EGU

158 $-2 \cdot Nit \cdot LgtlimN \cdot \hat{r}$

159 $-rOxNH_4 \cdot DecD2N \cdot \hat{r}$

157 $-SOC \cdot THK_{bot}$, (4)

160

161 A sedimentary particulate organic nitrogen (PON_{sed}) pool due to vertical sinking processes of PON was introduced for
162 parameterization of SOC. The SOC scheme is (Fennel et al., 2006) known as the instantaneous consumption of DO as soon as
163 the PON falls into the sediment bed, which tends to underestimate SOC at the peak of blooms and to overestimate SOC after
164 blooms since the lag in SOC demand is neglected (Fennel et al., 2013). We considered such temporal delays of SOC by
165 introducing a PON_{sed} pool. A portion of sinking PON ends up with PON_{sed}, while the rest is buried (PON_{burial}) and is removed
166 out of the system. The parameterization is shown in the following. 1) Organic matter settling down at the conceptual sediment
167 layer is remineralized at a temperature-dependent aerobic remineralization rate, K_{P2N}. 2) Sediment oxygen is consumed only
168 in the oxidation of sedimentary organic matter (represented by PON_{sed}) and the nitrification of ammonium to nitrate (Fennel
169 et al., 2006). 3) Oxygen consumption at the conceptual sediment layer directly contributes to decreases of oxygen concentration
170 only at the overlying water. 4) Sediment denitrification is linearly related to SOC according to observational-based estimates
171 by Seitzinger and Giblin (1996), but the relationship was modified by Fennel et al. (2006) with a slightly smaller slope of
172 denitrification on SOC rate, i.e.,

173 $denitrification\ (mmolN\ m^{-2}\ day^{-1}) = 0.105 \times SOC(mmolO_2\ m^{-2}\ day^{-1})$, (5)

174 5) Aerobic decomposition of PON_{sed} , sediment nitrification, and denitrification follow chemical equations according to
175 (Fennel et al., 2006):

176 $C_{106}H_{263}O_{110}N_{16}P + 106O_2 \leftrightarrow 106CO_2 + 16NH_4 + H_2PO_4 + 122H_2O$, (R1)

177 $NH_4 + 2O_2 \rightarrow NO_3 + 2H + H_2O$, (R2)

178 $C_{106}H_{263}O_{110}N_{16}P + 84.8HNO_3 \rightarrow 106CO_2 + 42.4N_2 + 16NH_3 + H_3PO_4 + 148.4H_2O$, (R3)

179

180 The linear assumption in 4) implicitly builds relationships among the reactions listed in assumption 5). We assumed that the
181 production rate of NH_4 by aerobic decomposition of organic matter is M mmol m^{-3} day^{-1}, and that the fraction of denitrification-
182 produced CO_2 to the total CO_2 production is x. According to the linear assumption abovementioned, we obtained $\frac{84.8Mx}{16(1-x)} =$
183 $0.105 \times \left[\frac{106M}{16} + \frac{84.8Mx}{8(1-x)}\right]$, yielding that $x \approx 0.1425$. The oxygen consumption rate (Eq. (6)) and organic matter consumption rate
184 (Eq. (7)) due to the coupled aerobic decomposition, nitrification, and denitrification processes were then obtained by
185 substituting the x value into the stoichiometric ratios according to Eq. (R1)–(R3).

186 $Oxyg_{consumption} = \frac{106M}{16} + \frac{84.8Mx}{8(1-x)} = 8.3865M$, (6)

187 $OM_{consumption} = \frac{M}{16} + \frac{Mx}{16(1-x)} = 0.0729M$, (7)

188 Accordingly, the SOC and consumption rate of PON_{sed} were given, respectively as follows:

https://doi.org/10.5194/bg-2022-3
Preprint. Discussion started: 11 January 2022


Biogeosciences Discussions Open Access EGU

$$SOC = Oxyg_{consumption} \cdot THK_{bot} = 8.3865M \cdot THK_{bot}, \quad (8)$$

$$PON_{sed_{consumption}} = 16 \cdot OM_{consumption} \cdot THK_{bot} = 1.1662M \cdot THK_{bot}, \quad (9)$$

where,

$$M = \frac{PON_{sed} \cdot VP2N_0 \cdot exp(K_{P2N} \cdot TMP)}{THK_{bot}}, \quad (10)$$

$$THK_{bot} = thickness\ of\ overlaying\ water, \quad (11)$$

For further comparison with the DO concentration, we transferred the SOC rate into a volume-based unit (mg L^{-1} day^{-1}) dividing the rate by $THK_{bot.}$ For simplification, the terminology of SOC was still applied to represent the transferred SOC rate in the following discussion. We further added light inhibition on nitrification (Olson, 1981) and oxygen dependency on nitrification and aerobic decomposition. These parametrizations were applied following descriptions by Fennel et al. (2006, 2013). For the oxygen-dependent term, an oxygen threshold was specified below which no aerobic respiration or nitrification occurred. Detailed equations were listed in Appendix A. The structure of the newly modified NEMURO model was shown in a schematic diagram in Figure 1.

https://doi.org/10.5194/bg-2022-3
Preprint. Discussion started: 11 January 2022

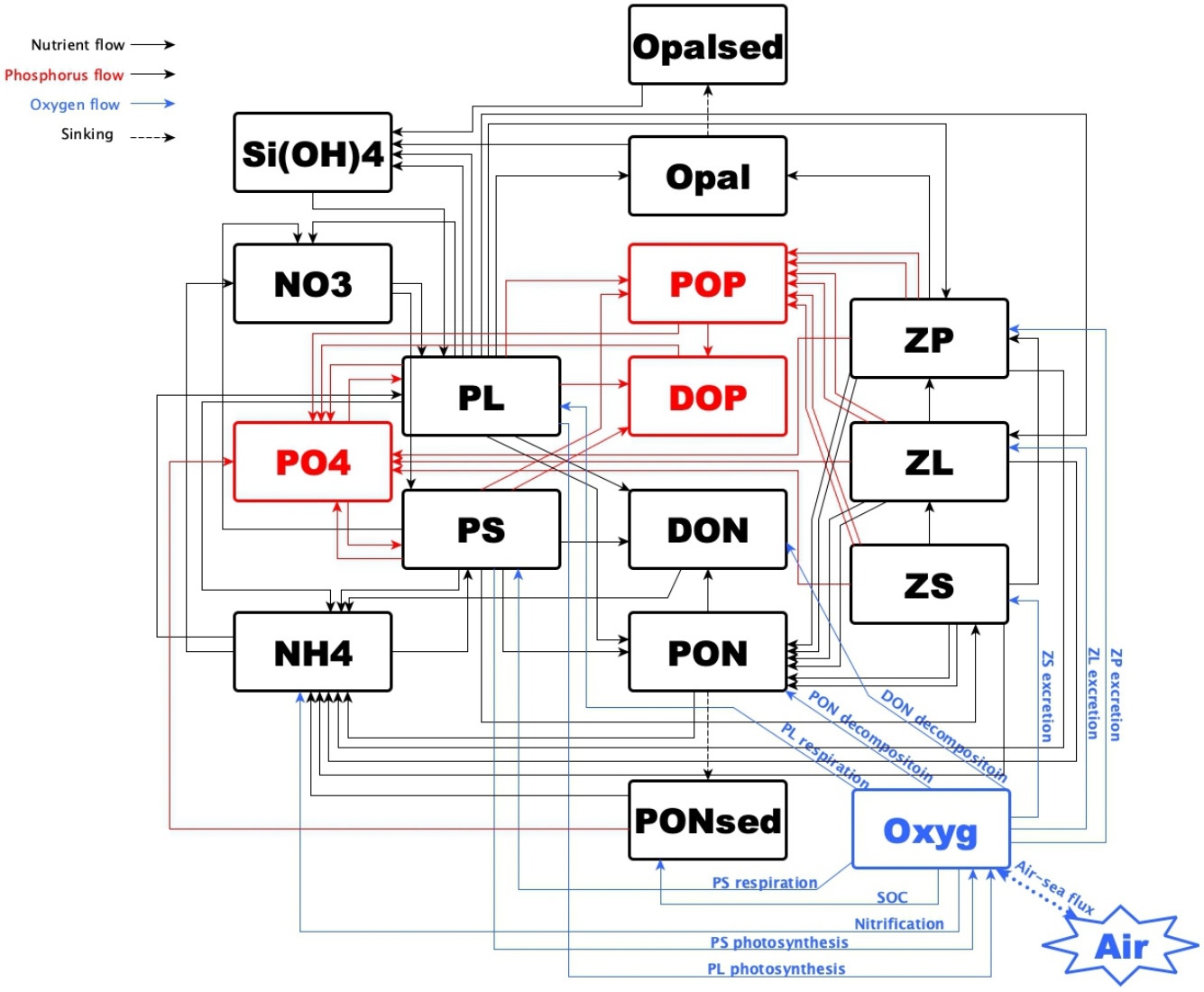

Figure 1. Schematic diagram of the modified NEMURO model. Note that the phosphorus flow and the oxygen flow are two newly added flows to the original NEMURO model.

2.3 Model set-ups

The coupled model was applied to the GoM using Arakawa C-grid with a horizontal resolution of ~5 km (Figure 2a). There are 334 and 357 interior rho points in east-west and north-south directions, respectively. The model includes 36 sigma layers vertically. The wetting and drying scheme (Warner et al., 2013) was implemented for a more accurate representation of shallow water. The computational time step (i.e., baroclinic time step) was set to be 240 seconds while the number of barotropic time steps between each baroclinic time step was set to be 30. Model hindcast was carried out from 1 August 2006 to 26 August 2020 with the first 5 months as a spin-up period. Model results were output on a daily interval at UTC 00: 00.

https://doi.org/10.5194/bg-2022-3
Preprint. Discussion started: 11 January 2022

The physical model set-ups largely followed an earlier Gulf–COAWST application (Zang et al., 2018, 2019, 2020). Open boundaries were set at the south and east forced by daily water level, horizontal components of 3-D current velocity, horizontal components of depth-integrated current velocity, 3-D water salinity, and 3-D water temperature derived from the Hybrid Coordinate Ocean Model (HYCOM) global analysis products (i.e., GLBu0.08 expt_19.1, GLBu0.08 expt_90.9, GLBu0.08 expt_91.0, GLBu0.08 expt_91.1, GLBu0.08 expt_91.2, GLBv0.08 expt_93.0, and GLBy0.08 expt_93.0, for detailed information, seeing https://www.hycom.org/hycom) (Cummings, 2005; Cummings and Smedstad, 2013; Fox et al., 2002; Helber et al., 2013). For lateral boundary conditions, we utilized Chapman implicit for free surface and water level (Chapman, 1985), Flather for depth-integrated momentum (Flather, 1976), gradient for mixing total kinetic energy, and mixed radiation-nudging conditions for 3-D momentum, temperature, and salinity (Marchesiello et al., 2001). The nudging time steps for the mixed radiation-nudging condition were set to 1 day for inflows and 30 days for outflows. The boundary nudging technique was performed at the computational grids along the open boundary. The boundary condition types for biochemical passive tracers (i.e., PS, PL, ZS, ZL, ZP, NO_3, NH_4, PON, DON, $Si(OH)_4$, opal, PO_4, POP, DOP, and Oxyg) were all prescribed as radiation.

Initial conditions for water level, horizontal components of 3-D current velocity, horizontal components of depth-integrated current velocity, 3-D water salinity, and 3-D water temperature were provided by the same HYCOM products as well. Initial conditions for concentrations of NO_3, PO_4, and $Si(OH)_4$ were interpolated from measurements provided by the World Ocean Database (WOD, Boyer et al., 2018). Initial conditions for DO concentration were given by World Ocean Atlas (WOA, Garcia et al., 2018). Other biochemical tracers were initialized as 0.1 mmol m^{-3} due to the lack of observations.

Atmospheric forcings, including surface wind velocity at 10 m height above sea level, net longwave radiation flux, net shortwave radiation flux, precipitation rate, air temperature 2 m above sea level, sea surface air pressure, and relative humidity 2 m above sea level, were derived from the National Centers for Environmental Prediction (NCEP) Climate Forecast System Reanalysis (CFSR) 6-hourly products (for years prior to 2011, Saha et al., 2010) and NCEP CFS Version 2 (CFSv2) 6-hourly products (for years starting from 2011, Saha et al., 2011) with a horizontal resolution of ~35 km and ~22 km, respectively. In our model, 63 rivers were considered as horizontal point source forcings along the coastal GoM. They were split into 280 point sources transporting time-varying salinity (nearly zero), temperature, 3-D horizontal momentum (based on the magnitude of river discharges), nutrients (NO_3, NH_4, PO_4, $Si(OH)_4$, PON, DON, POP, and DOP), and DO to the computational domain. Locations of river point sources of the Mississippi and the Atchafalaya Rivers are shown as red dots in Figure 2b. For reconstructions of time series of river forcing terms, we composed measurements from various sources including U.S. Geological Survey (USGS) National Water Information System (NWIS), National Oceanic and Atmospheric Administration (NOAA) Tides and Currents System (TCS), NOAA National Estuarine Research Reserve System (NERRS), and Mexico National Water Commission (CONAGUA, for rivers in Mexico's territory). Daily averaged river discharges were given based on measurements by USGS NWIS and CONAGUA. The magnitude of river discharges was multiplied by 1.4 to account for

https://doi.org/10.5194/bg-2022-3
Preprint. Discussion started: 11 January 2022

246 adjacent watershed areas and lateral inflow of tributaries (Warner et al., 2005). River temperature and salinity time series were
247 reconstructed from measurements by USGS NWIS, NOAA TCS, and NOAA NERRS. River nutrient concentrations were
248 provided monthly by USGS NWIS and NOAA NERRS and were extended to daily time series with values in the corresponding
249 months. Riverine DO concentration was set to be a constant (511 mmol m^{-3}) assuming that riverine DO was highly
250 oversaturated. Besides, tidal forcings were introduced in the hydrodynamic model taking into account of influences of tidal
251 elevations and tidal currents. There were 13 tidal constituents considered in the model including M2, S2, N2, K2, K1, O1, P1,
252 Q1, MF, MM, M4, MS4, and MN4.
253

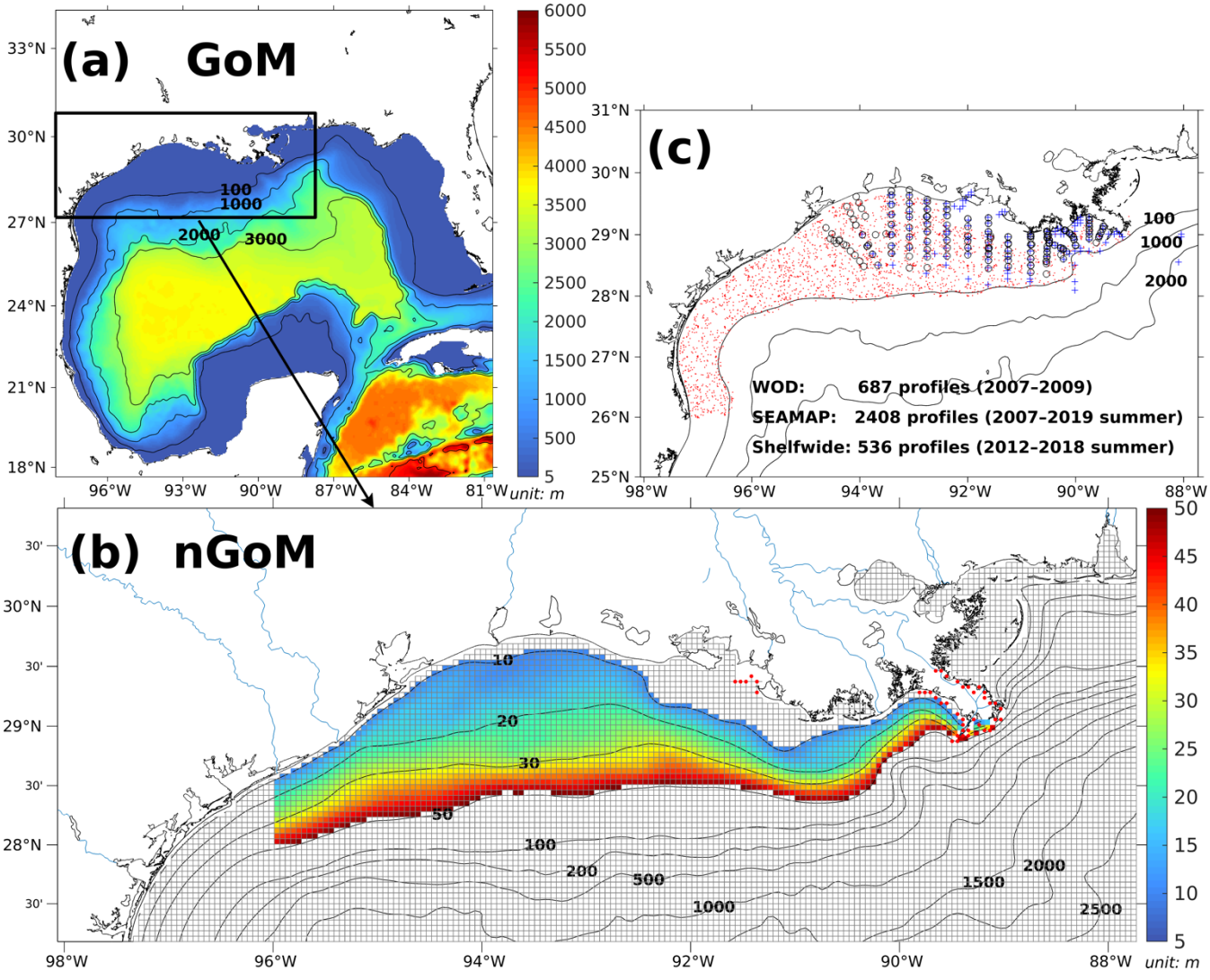

254
255 **Figure 2. (a) Bathymetry of the entire domain of the Gulf–COAWST, (b) zoom-in bathymetry plot of the northern Gulf of Mexico**
256 **(nGoM), and (c) locations of observed inorganic nutrient and DO profiles derived from WOD, SEAMAP, and midsummer Shelfwide**
257 **cruises. In (b), only bathymetry between 10 and 50 m was mapped with colors; computational meshes were split by solid grey lines;**

https://doi.org/10.5194/bg-2022-3
Preprint. Discussion started: 11 January 2022


Biogeosciences Discussions Open Access EGU

main river channels are denoted by solid blue curves; locations of river point sources of the Mississippi and the Atchafalaya Rivers were indicated by red dots. In (c), locations of profiles by WOD, SEAMAP, and midsummer Shelfwide cruises are denoted by blue crosses, red dots, and black circles, respectively.

3 Biogeochemical model validations

In this section, profile comparisons between model results and observations from various sources were conducted for concentrations of NO_3, PO_4, $Si(OH)_4$, and DO. Model simulated profiles were linearly interpolated to the specific depth of the observed profiles for a quantitative comparison. We also provided detailed comparisons of frequency distributions of hypoxic thickness, spatial distributions of bottom DO, and temporal variability of the hypoxic area between the model results and the Shelfwide measurements. Validation of the hydrodynamic model can be found in Zang et al. (2019).

3.1 Available measurements

Inorganic nutrient concentration profiles from WOD were used for model validation. Measurements cover a period from 11 January 2007 to 5 July 2009 including 436 NO_3 profiles, 377 PO_4 profiles, and 215 $Si(OH)_4$ profiles. Available DO concentration profiles were obtained from the WOD, NOAA-supported midsummer Shelfwide cruises, and Summer Groundfish Survey in GoM supported by Southeast Area Monitoring and Assessment Program (SEAMAP) and conducted annually by the Gulf States Marine Fisheries Commission. There were 410 DO profiles (11 January 2007 to 5 July 2009) available provided by WOD. There were at least 77 DO profiles for each summer (July–August for years 2012, 2013, 2014, 2015, 2017, and 2018) derived from the Shelfwide cruises observations. More than 3,000 measurements were conducted each summer except 2017 summer (909 in total) by Shelfwide cruises. Selected SEAMAP summer DO measurements covered a time range from 2007 to 2019 with higher data coverage (152–331 DO profiles including 4,141–12,550 measurements for each summer) than the WOD and Shelfwide observations. Locations of the selected profiles from different archives are shown in Figure 2c. We estimated the hypoxia thickness (Figure 5) and spatial extents of bottom hypoxic water (Figure 6) based on the Shelfwide DO profiles measurements. The observed spatial patterns were obtained by interpolating the measured bottom DO concentration to the computational grids. Time series of summer hypoxic areas estimated by the Shelfwide cruises were available from 2008 to 2020 with a range from 5,480 km^2 to 22,720 km^2 (https://gulfhypoxia.net/research/shelfwide-cruises/, Figure 7).

3.2 Inorganic nutrients concentration profiles

WOD-derived and modeled nutrient profiles show a good agreement in terms of vertical distributions and magnitudes (Figure 3). Both simulations and measurements are relatively higher in shallow water areas (within 10 m). Higher PO_4 and $Si(OH)_4$ concentrations were found at the lower water layers for both simulated and measured profiles in waters deeper than 10 m. Nonetheless, NO_3 and PO_4 concentration were both slightly overestimated by the model, while $Si(OH)_4$ concentration was marginally underestimated. The probability histogram of NO_3 concentration differences between simulations and

https://doi.org/10.5194/bg-2022-3
Preprint. Discussion started: 11 January 2022

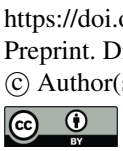

measurements illustrates that ~60 % of total simulation–measurement pairs drop within a range from -10 to 10 mmol m^{-3} with ~40 % in the positive interval (i.e., from 0 to 10 mmol m^{-3}). The same statistics were also found for PO_4 comparisons within a range of ±0.4 mmol m^{-3}. However, there were ~15 % of observed $Si(OH)_4$ being overestimated by within 10 mmol m^{-3} and ~50 % being underestimated by within 10 mmol m^{-3}. Mean NO_3 concentrations from the Mississippi and the Atchafalaya Rivers were 99 ± 34 mmol m^{-3} (mean ± 1sd) and 66 ± 29 mmol m^{-3}, respectively. Similarly, mean riverine PO_4 concentrations were found as 2.7 ± 0.7 mmol m^{-3} and 2.3 ± 0.7 mmol m^{-3}, respectively, and mean riverine $Si(OH)_4$ concentrations were 118 ± 23 mmol m^{-3} and 116 ± 21 mmol m^{-3}, respectively. The nutrient concentrations bias between simulations and observations are therefore acceptable concerning the strong influences of high riverine nutrient loadings on the shelf waters.

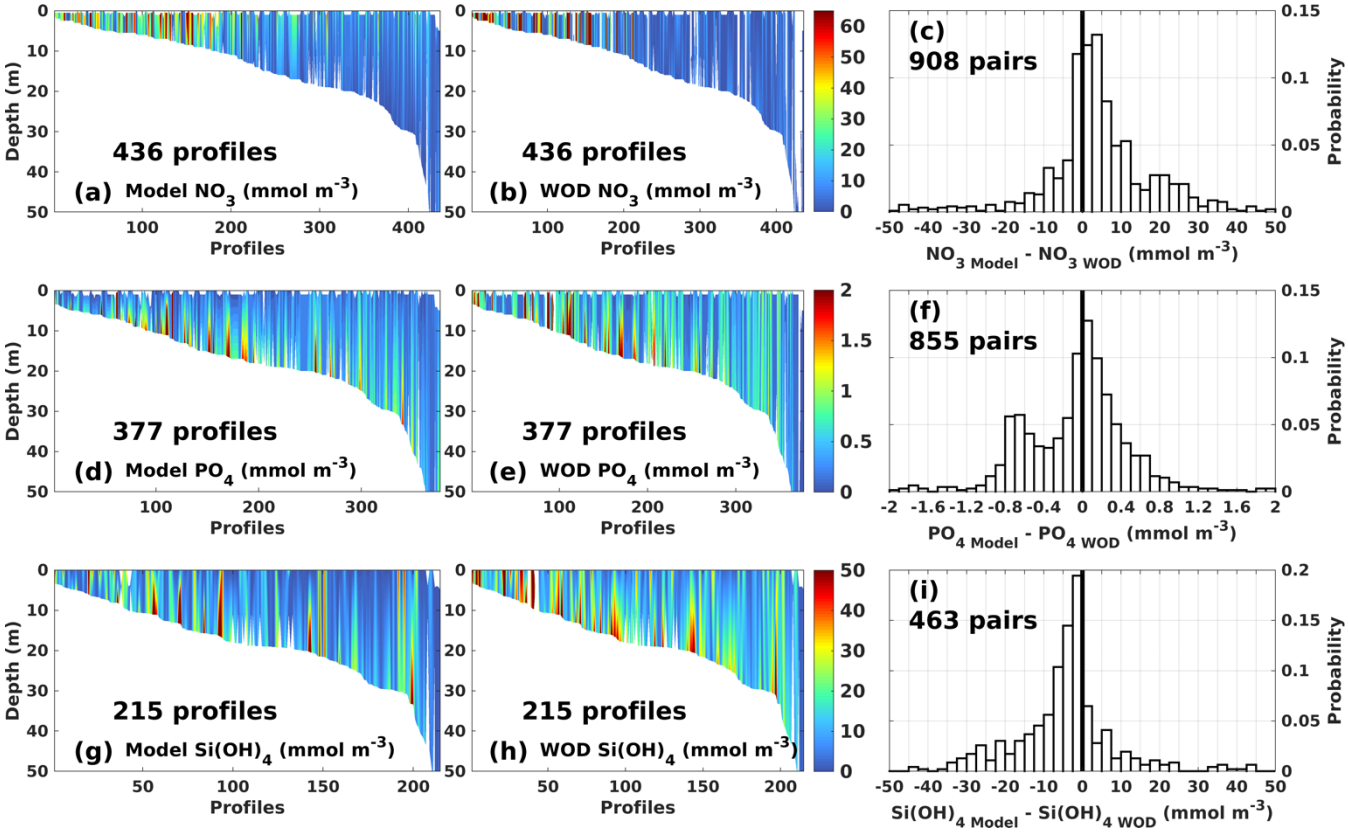

Figure 3. Profile comparisons between model hindcasts and WOD measurements for concentrations of (a)–(c) NO_3, (d)–(f) PO_4, and (g)–(i) $Si(OH)_4$. Note that the thick vertical lines in (c), (f), and (i) denote the concentration difference of 0 separating the positive and negative intervals.

3.3 DO concentration profiles

DO decreases from the upper to the lower water layers in both simulated and WOD profiles (Figures 4a–4b). Hypoxia was mainly detected in profiles with depth between 10 m and 20 m. Hypoxia was more frequent as shown in the WOD DO profiles, indicating that the model overestimated the observed DO (Figures 4a–4c). The total number of model–measurement relative percentage difference pairs is 901, ~72 % of which are within a range of ±50 %. Our model overestimated/underestimated ~32

https://doi.org/10.5194/bg-2022-3
Preprint. Discussion started: 11 January 2022

%/~19 % of total DO observations by within 20 % and overestimated/underestimated ~21 %/14 % of total DO observations by within 10 %.

In both modeled and NOAA's Shelfwide DO profiles, massive hypoxic events were detected mainly in profiles with depth from 10 to 20 m (Figures 4d–4e). The probability histogram of DO relative percentage differences between simulations and observations shows a bell-shaped distribution with a peak around zero. There were ~30 %, ~44 %, and ~67 % of observations being misestimated by within ±10 %, ±20 %, and ±50 %, respectively (Figure 4f). Model results showed a good agreement with the Shelfwide observations.

Due to the data discontinuity before 2012 and after 2018 provided by WOD and Shelfwide cruises, summer DO profiles measurements by SEAMAP were used for DO validation as well (Figures 4g–4i). Our model well captured the magnitude and vertical structures of observed DO in each summer, although slight overestimations existed. There were ~52 %, ~75 %, ~93 % of total relative difference pairs dropping within a range of ±10 %, ±20 %, and ±50 %, respectively.

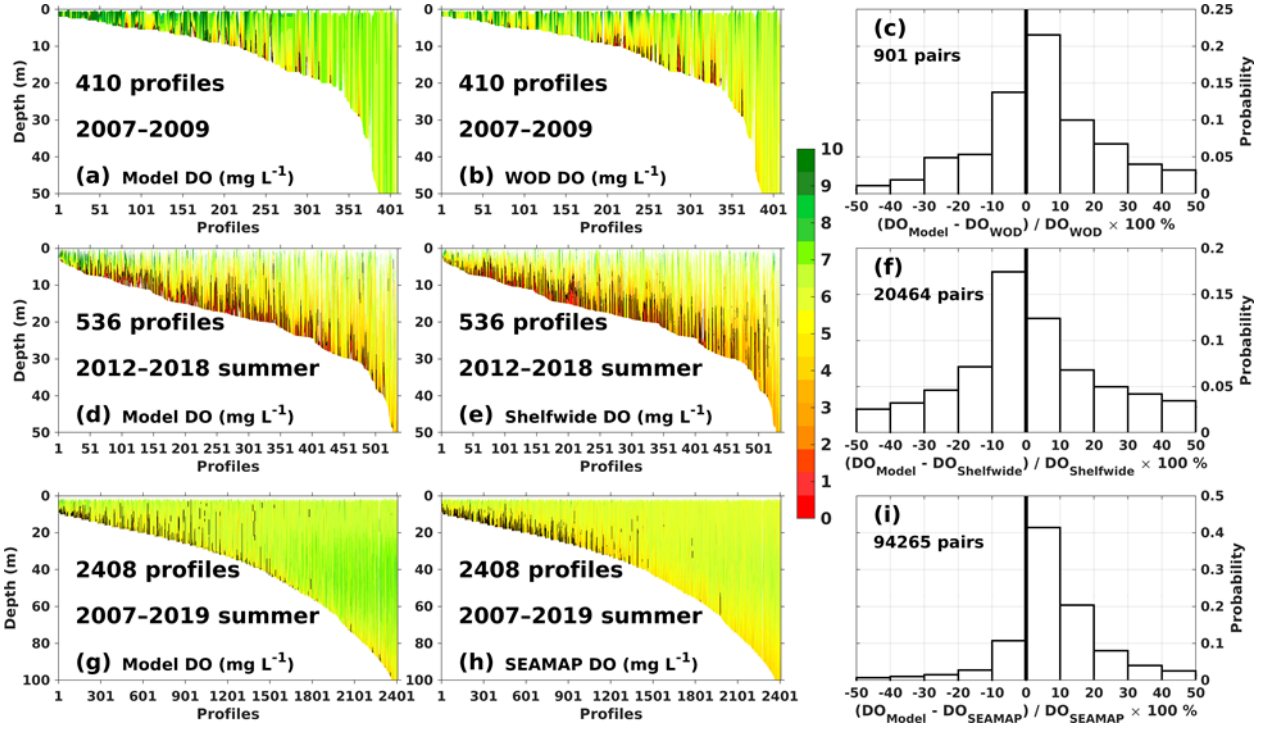

Figure 4. Comparisons of DO profiles between model hindcasts and measurements by (a–c) WOD, (d–f) NOAA's summer Shelfwide cruises, and (g–i) SEAMAP. Figures 4c, 4f, and 4i show the distribution of relative percentage differences between modeled and observed DO. The solid black contour lines in the profile plots represent the DO concentration of 2 mg L^{-1}. The thick vertical lines in the histograms denote the percentage difference of 0.

https://doi.org/10.5194/bg-2022-3
Preprint. Discussion started: 11 January 2022


Biogeosciences Discussions

3.4 Hypoxic thickness, spatial distributions of bottom DO, and temporal variability of hypoxic area

Previous studies pointed out that hypoxic volume needs to be considered along with the hypoxic area as another metric in model's ability assessments (Fennel et al., 2016; Scavia et al., 2019). The thickness of hypoxia layers was thus estimated here by integrating the thickness of water layers where DO concentration was ≤ 2 mg L^{-1} starting from the bottom water layer. NOAA's Shelfwide measurements found 210 out of the 536 DO profiles contain hypoxia, and the model simulated 225 (Figure 5). Modeled hypoxia thickness exhibits a similar right-skewed distribution as the observations. The thickness of 1–2 m was found most prevalent in both measured and simulated results. Hypoxia thickness was found ≤ 4 m in 66 % of observed profiles and 77 % of modeled profiles. Results suggest that our model can well reproduce the observed hypoxia thickness.

Model simulated bottom DO was resampled following the periods covered by the Shelfwide cruises during each summer. Simulated results outside the LaTex Shelf and over the deep (> 100 m) and shallow (< 10 m) water regions were excluded since observations were unavailable over these regions. Numerical results show a good agreement with the observations in terms of interannual variability and extent of bottom hypoxic waters (Figure 6). Except for the 2013 summer, no hypoxia was detected at waters deeper than 50 m by either cruises or the model. The spatial distribution of the hypoxic regions varies over different summers. For example, the hypoxic extent was small and was mostly restricted in nearshore (<20 m) regions during summers of 2012 (Figures 6a–6b) and 2018 (Figures 6k–6i). However, the extent was much larger with a more offshore outreach in 2013 (Figures 6c–6d) and 2017 (Figures 6i–6j) but a more nearshore distribution in 2014 (Figures 6e–6f) and 2015 (Figures 6g–6h). The spatial dispersion of hypoxic waters occurs mostly over the west of the LaTex Shelf where bathymetry gradients are gentle. Over the eastern shelf, the hypoxic water is mostly constrained within a narrow belt. In the meantime, the western and eastern hypoxic water are not always merged but are separated at around 91 °W (e.g., 2012, 2014, 2015, and 2018). These results suggest that LaTex Shelf can be split according to bathymetry and distances from the major river mouths (Figure 8d). The above features were found in both the numerical results and cruises observations, suggesting that the model can well reproduce the spatial patterns of bottom DO.

The daily time series of the hypoxic area was calculated over the LaTex Shelf with depth from 10 to 50 m (Figure 7). Summer hypoxic area shows a good agreement between simulations and Shelfwide cruises measurements in terms of magnitude and variability. Our model tended to underestimate the measurements in 2008, 2010, 2012, 2017, and 2020 and to overestimate in other summers of interest. Nevertheless, those biases are acceptable considering the relative sporadic converges of cruises data.

https://doi.org/10.5194/bg-2022-3
Preprint. Discussion started: 11 January 2022

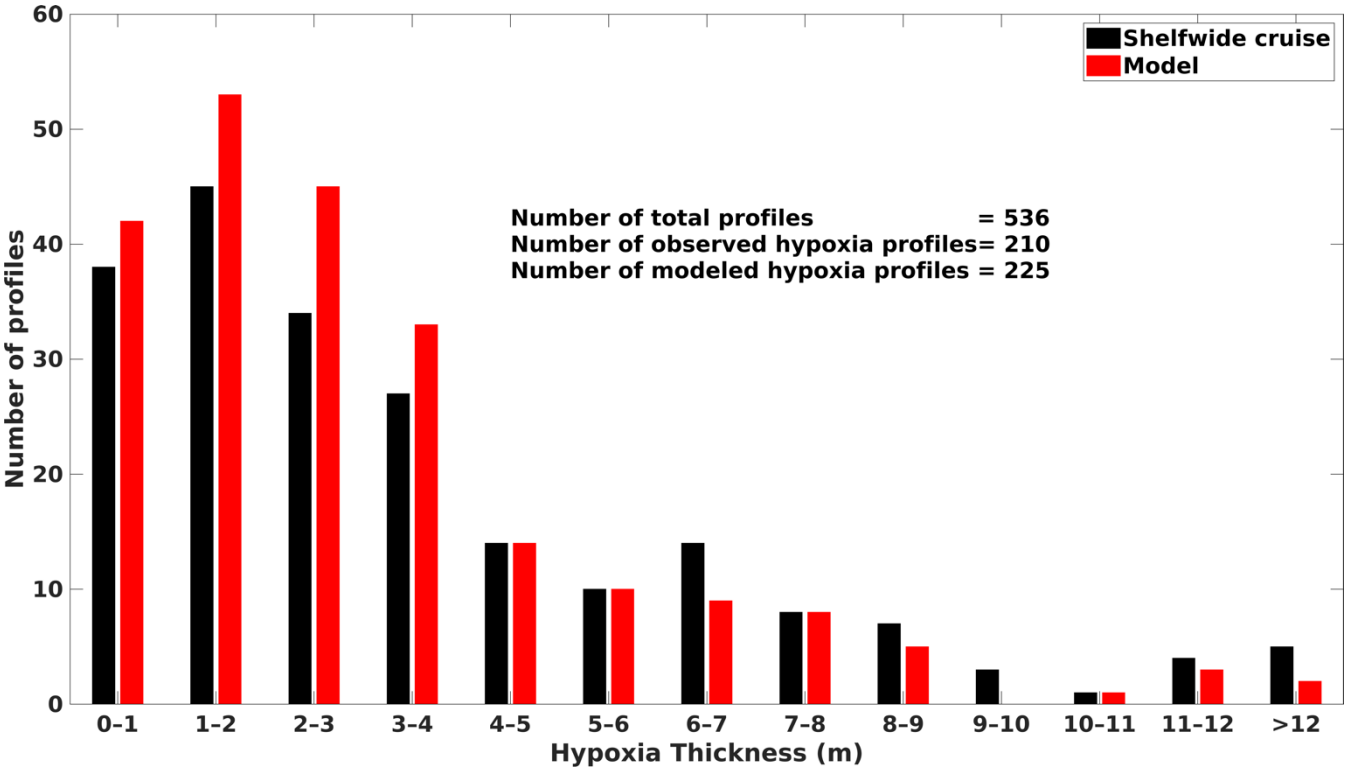

Figure 5. Frequency distribution of hypoxia thickness obtained from NOAA's Shelfwide cruises measurements and model results during the Shelfwide summer investigation periods from 2012 to 2018 (except 2016).

https://doi.org/10.5194/bg-2022-3
Preprint. Discussion started: 11 January 2022

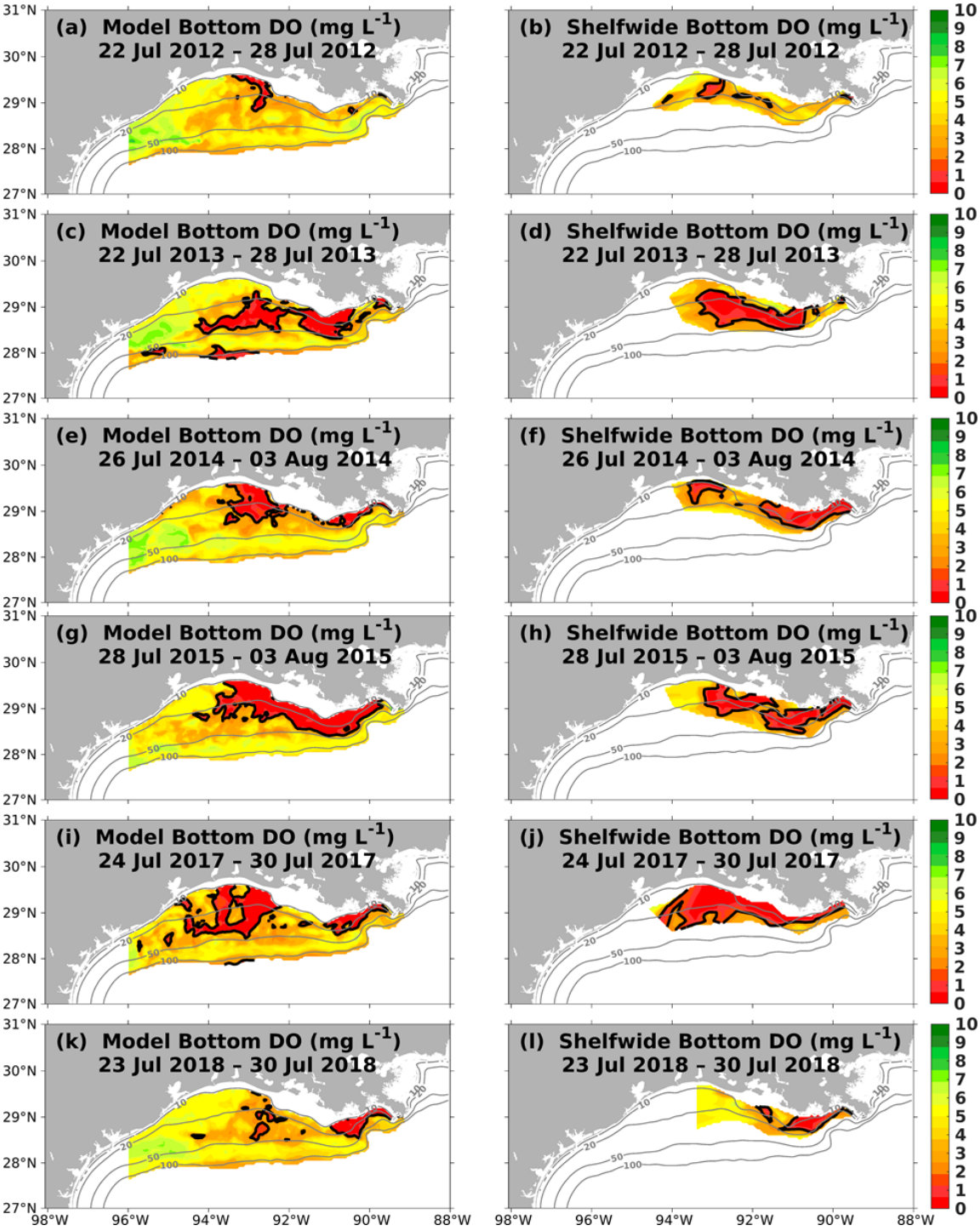

Figure 6. Summer blended bottom DO concentration from model results (left panels) and NOAA's Shelfwide observations (right panels). The solid grey lines indicate bathymetry of 10, 20, 50, and 100 m, while the solid black lines represent isolines of DO concentration of 2 mg L^{-1}.

https://doi.org/10.5194/bg-2022-3
Preprint. Discussion started: 11 January 2022

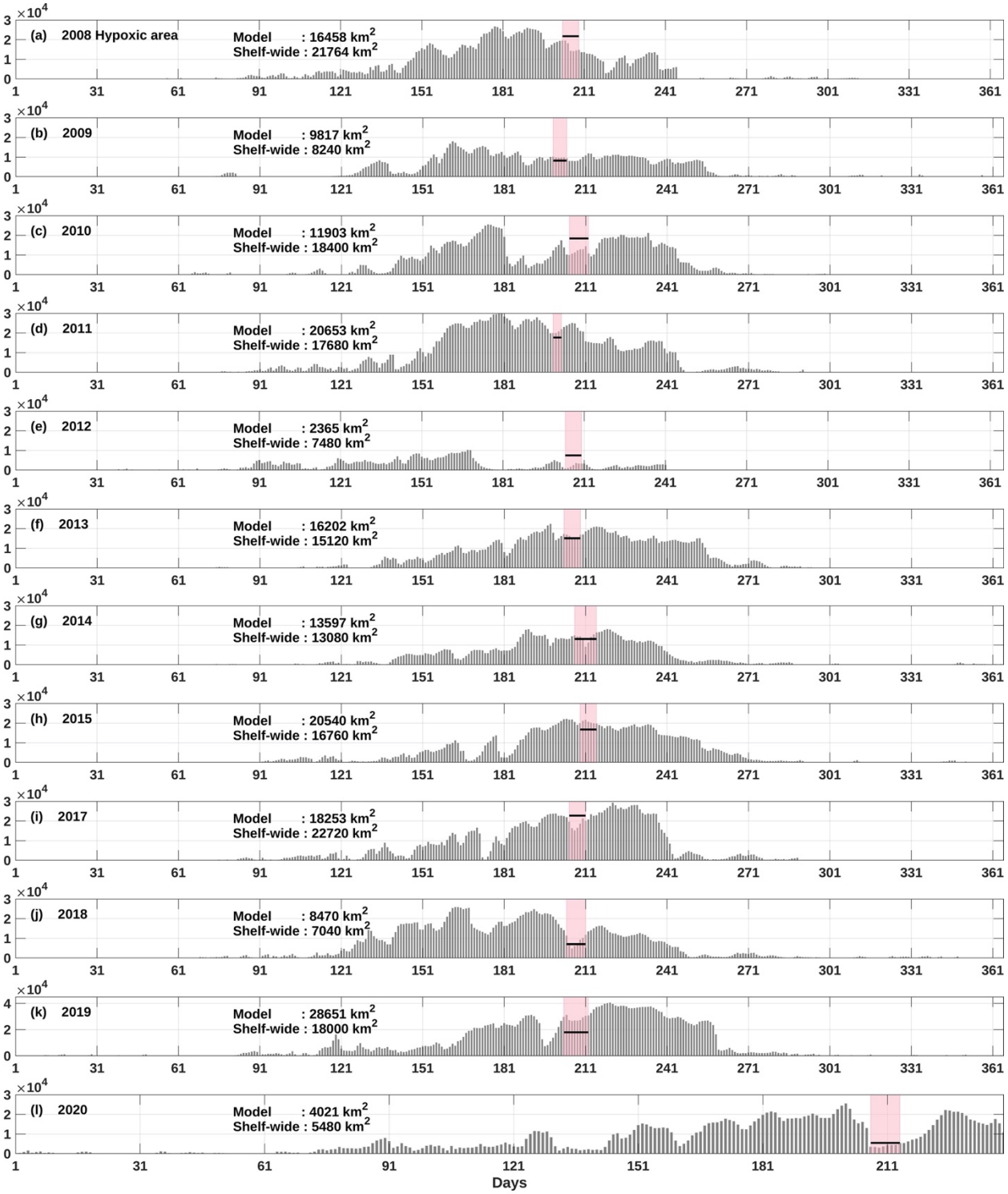

Figure 7. Comparison of the hypoxic area (in km^2) between model simulations and Shelfwide cruises observations from 2008 to 2020 (except 2016). The pink patches denote the cruises periods while the solid black lines represent the measured hypoxic area.

https://doi.org/10.5194/bg-2022-3
Preprint. Discussion started: 11 January 2022

4 Results and discussion

4.1 Characteristics of bottom DO in LaTex Shelf

The above analysis suggests that the shelf can be split according to bathymetry and distances from the major river mouths for mechanism study. Therefore, also referring to Fennel et al. (2016), the shelf within 50 m isobath was divided into six subregions for the below analysis (Figure 8d). According to the distances to the two main river systems (i.e., the Mississippi and the Atchafalaya Rivers), from east to west the LaTex Shelf was split into two west-Mississippi regions (10–20 m nearshore and 20–50 m offshore regions, similar hereinafter), two mid-Atchafalaya regions, and two west-Atchafalaya regions. Over the entire shelf, multiyear mean (2007–2020) of bottom DO concentration ranges from 3 to 7 mg L^{-1} with a regional mean of 5.6 mg L^{-1} (Figure 8a). A remarkable southwestward gradient manifests the impacts from river plumes and Louisiana coastal currents. Linear long-term trends (Figure 8b) and standard deviations (STDs, Figure 8c) were obtained at every computational grid based on the daily bottom DO concentration results. The bottom DO concentration exhibits an overall negative long-term trend with a maximum decrease rate of 0.15 mg L^{-1} yr^{-1} identified in the mid-Atchafalaya nearshore region (Figure 8b). The STDs of detrended bottom DO concentration show an uneven spatial distribution over the shelf (Figure 8c). The STDs are greater than 2 mg L^{-1} mostly in nearshore regions. The maximum STDs were found at the west-Mississippi and mid-Atchafalaya nearshore regions where multi-year averages are the minimum among the six subregions.

Daily climatology (spatially averaged over the color shaded area in Figure 8d, same hereinafter) of bottom DO concentration and hypoxic area are negatively correlated over a year (Figure 8e). The bottom DO concentration starts to decrease dramatically at the beginning of May followed by a trough of ~3 mg L^{-1} in July and August and a fast rebound in September. Correspondingly, the hypoxic area increases remarkably in early May followed by a peak of ~17,200 km^2 in July and August and a dramatic shrinkage in September. May, June, July, and August are the most affected months by hypoxic events. Monthly climatology results show different evolution patterns of bottom hypoxia in the west and east shelf (Figures 9a, 9c, 9e, and 9g). Bottom DO concentrations reach below the hypoxic threshold of 2 mg L^{-1} in May over the mid-Atchafalaya nearshore region. Low DO area then extends offshore reaching the 20 m isobath in June. In July, mid-Atchafalaya nearshore hypoxic waters propagate south-eastward while the west-Mississippi nearshore waters start to become massively hypoxic. In August, the west hypoxic waters reach more south-eastward than in July merging with the east hypoxic waters. A longitudinally elongated hypoxia belt within the 50 m isobath is eventually formed.

https://doi.org/10.5194/bg-2022-3
Preprint. Discussion started: 11 January 2022

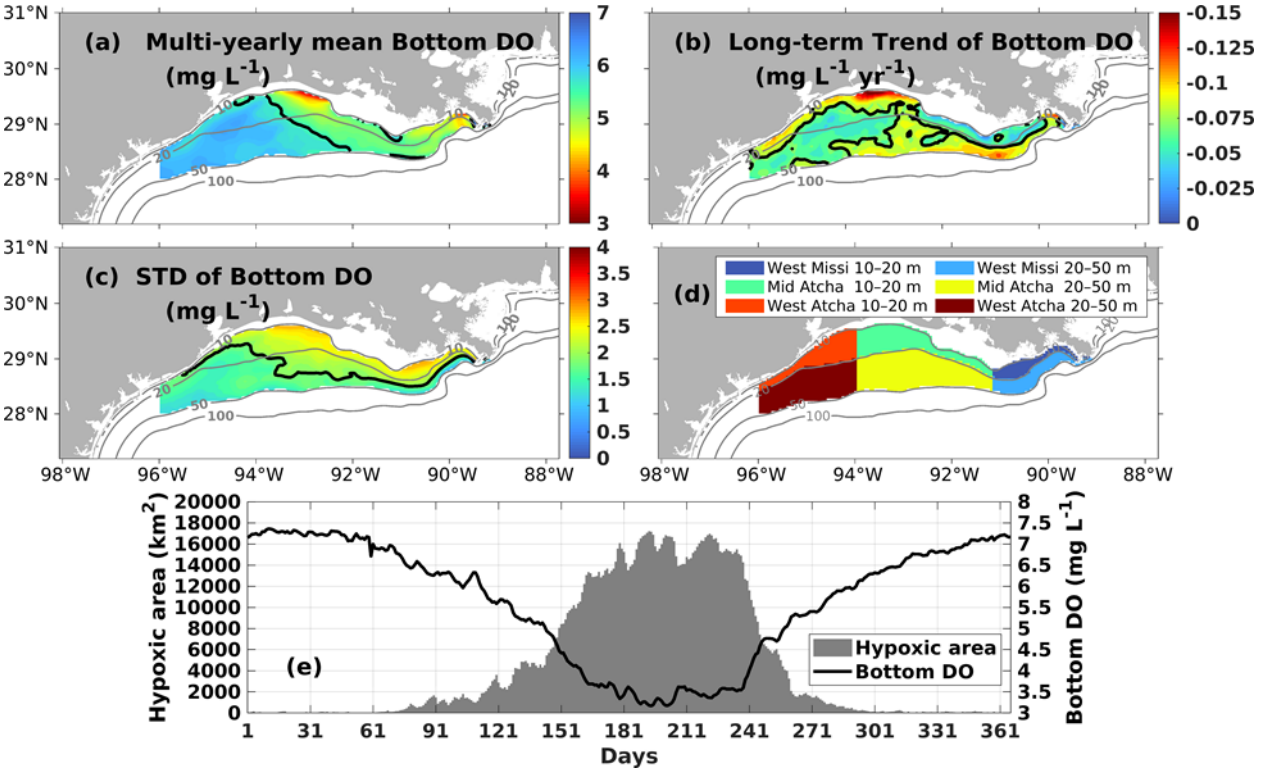

Figure 8. Spatial patterns of (a) multiyear (2007–2020) mean of, (b) linear long-term trend of, and (c) standard deviation (STD) of daily bottom DO concentration. (d) Subregions defined by Fennel et al. (2016). (e) Daily climatology (spatially averaged over the LaTex Shelf of 10–50 m) of hypoxic area and bottom DO concentration. The solid grey lines in (a)–(d) indicate bathymetry of 10, 20, 50, and 100 m. The solid black lines in (a), (b), and (c) represent the corresponding regionally averaged values of 5.6 mg L^{-1}, -0.067 mg L^{-1} yr^{-1}, and 1.9 mg L^{-1}, respectively.

For a given grid point, hypoxia percentage frequencies for May, June, July, and August were given based on occurrences of hypoxic events over the total length of days of the corresponding months (e.g., 434 days for May from 2007 to 2020) (Figures 9b, 9d, 9f, and 9h). The evolution of high hypoxia frequency (≥ 50 %) coverage behaves similarly to the evolution of hypoxic extent. The mid-Atchafalaya nearshore region is the most frequently affected domain by hypoxia in June, while the west-Mississippi nearshore region has the most hypoxia events in August. In July, both the two regions encounter high hypoxia occurrences with averaged percentages of 56 % and 63 %, respectively. More hypoxia events were simulated over the west-Mississippi offshore and mid-Atchafalaya offshore regions in July and August (frequency ≥ 20 %) than in other summer months.

The above results indicate that the evolution of bottom DO concentration in different subregions has its own characteristics. Bottom DO concentration in the west-Mississippi nearshore and mid-Atchafalaya nearshore regions seem to be more sensitive to the river systems with much lower mean values, higher STDs, and higher long-term decreasing rates. Even along the nearshore waters, the evolution of bottom hypoxia exhibits different patterns. For example, the time lag of the lowest bottom

https://doi.org/10.5194/bg-2022-3
Preprint. Discussion started: 11 January 2022

DO concentration (also the highest hypoxia percentage frequency) between the mid-Atchafalaya nearshore region and the west-Mississippi nearshore region was detected in the summer months. We further calculated the daily climatology of bottom DO concentration over different subregions and found a stronger seasonal pattern in the nearshore regions than in the offshore regions (Figure 10). Different time points when bottom DO concentration reaches minimum were detected in the two river plume areas. In the mid- and west-Atchafalaya nearshore regions, the bottom DO concentration reaches the trough in early June and starts to rebound in August. However, in the west-Mississippi nearshore region, concentration hits the minimum at the end of August followed by a fast rebound in September. Similar patterns can also be found in the offshore regions. Evidence indicates that modulation mechanisms on the variability of bottom DO concentration are different among these regions.

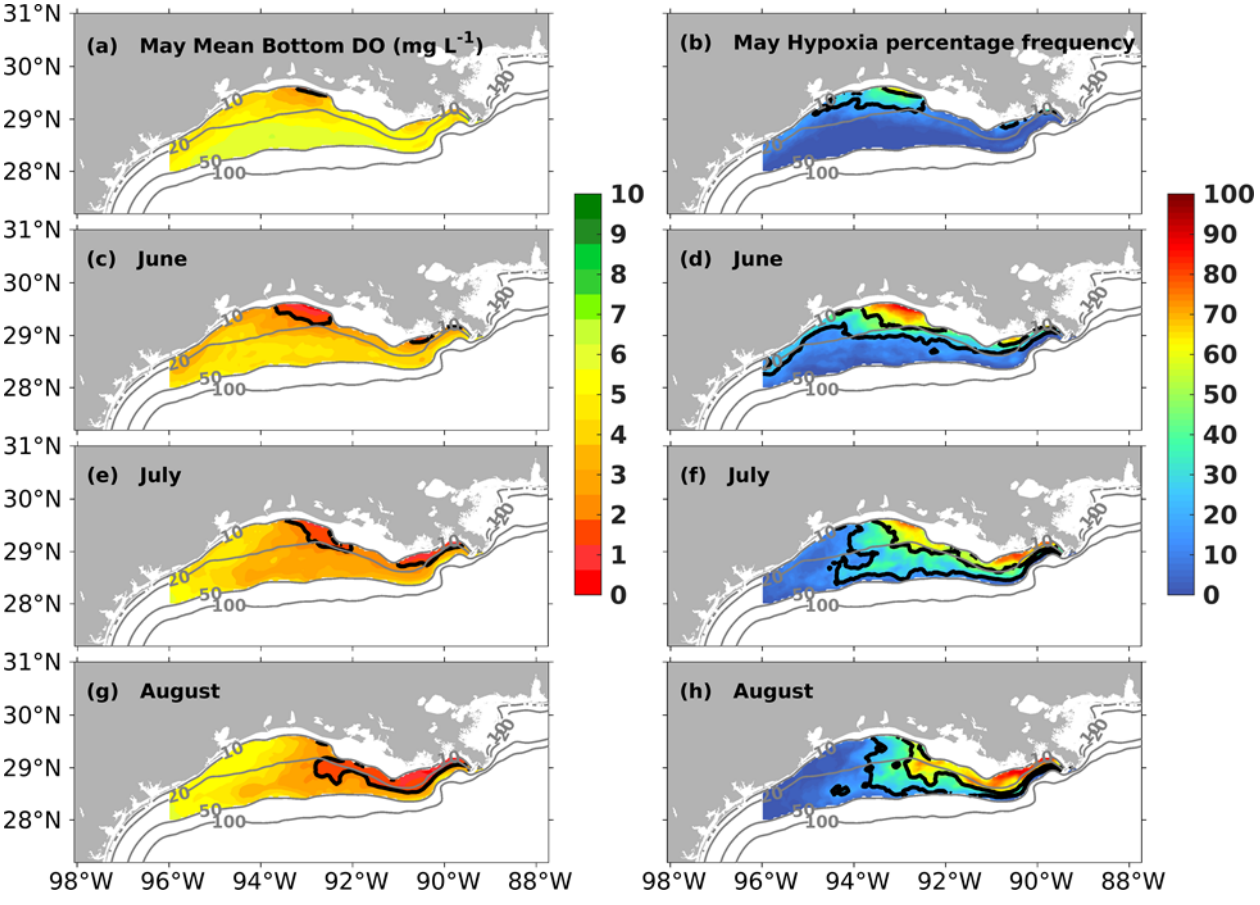

Figure 9. Spatial distribution of monthly climatology (May–August) of (left panel) bottom DO concentration and spatial distribution of (right panel) hypoxia percentage frequency for different summer months. The black solid lines in the left panel denote isolines of 2 mg L^{-1}, while those in the right panel represent isolines of 20 % and 50 %, respectively.

https://doi.org/10.5194/bg-2022-3
Preprint. Discussion started: 11 January 2022

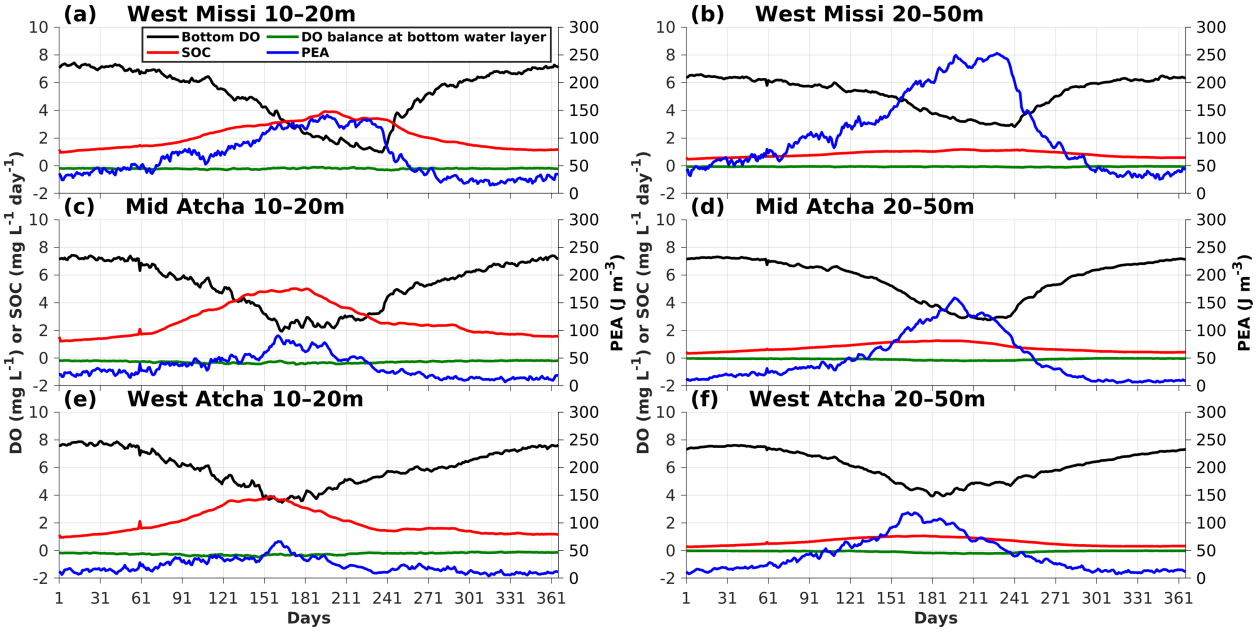

Figure 10. Time series of daily climatology (spatially averaged) of bottom DO concentration, SOC, DO balance term at the bottom water layer, and PEA over the (a) west-Mississippi nearshore region (10–20 m), (b) west-Mississippi offshore region (20–50 m), (c) mid-Atchafalaya nearshore region, (d) mid-Atchafalaya offshore region, (e) west-Atchafalaya nearshore region, and (f) west-Atchafalaya offshore region. Note that the DO balances at the bottom water layer only account for the biochemical processes occurring at the bottom water layer.

4.2 Sources and sinks of bottom DO

The dynamics of bottom DO concentration are controlled jointly by hydrodynamic processes, biochemical processes at the water–sediment interface, and biochemical processes at the overlying water. In this section, we aimed to compare the effects of these processes in different subregions.

4.2.1 Biochemical processes

SOC was estimated combining processes of aerobic mineralization, nitrification, and denitrification and was a critical sink of bottom DO. The monthly climatology of SOC starts to increase in May and reaches the maximum in June followed by a continuous decrease in July and August (Figures 11a, 11c, 11e, and 11g). The mid-Atchafalaya nearshore region is not only the SOC maximum zone during summer but also an area with greater SOC variability. Such features can also be found in the monthly climatology of bottom DO concentration and hypoxia frequency (Figure 9). The SOC isolines of 2 mg L^{-1} day^{-1} roughly follow the 20 m isobath, especially in the west-Mississippi region, indicating that bottom DO in offshore regions is less affected by sediment biochemical processes.

Time series of daily climatology of SOC over the six subregions (red solid curves in Figure 10) suggest that sediment biochemical processes are much more important in the nearshore regions than in the offshore regions in terms of modulating

https://doi.org/10.5194/bg-2022-3
Preprint. Discussion started: 11 January 2022

bottom DO variability. SOC in the offshore regions is generally lower than 1.5 mg L^{-1} day^{-1} with no apparent variation over a year, while SOC in the nearshore regions is much greater reaching high up to 5 mg L^{-1} day^{-1} during summer with a salient annual cycle. In the mid- and west-Atchafalaya nearshore regions, the timepoints of SOC peaks (5 mg L^{-1} day^{-1} and 4 mg L^{-1} day^{-1}, respectively in early June) are consistent with the timepoints of bottom DO troughs. The bottom DO in the west-Mississippi nearshore region decreases continuously from May to August, which seems to be modulated by not only SOC but also water stratification.

The oxygen balance at bottom water layers is determined by local oxygen sources from phytoplankton photosynthesis and local oxygen sinks through phytoplankton respiration, zooplankton metabolism, aerobic decomposition of PON and DON, and nitrification. The monthly climatology (Figures 11b, 11d, 11f, and 11h) suggests that the combined effects of these processes generally serve as a DO sink at the bottom layer from May to August. However, the contributions are limited with the maximum DO sink of 0.9 mg L^{-1} in May. Similarly, the time series of daily climatology shows near-zero DO balance over the studied subregions (Figure 10). Accordingly, the impacts of biochemical processes at the bottom water layer to the bottom DO dynamics are negligible. Results are consistent with previous incubation studies (Murrell and Lehrter, 2011; McCarthy et al., 2013).

https://doi.org/10.5194/bg-2022-3
Preprint. Discussion started: 11 January 2022

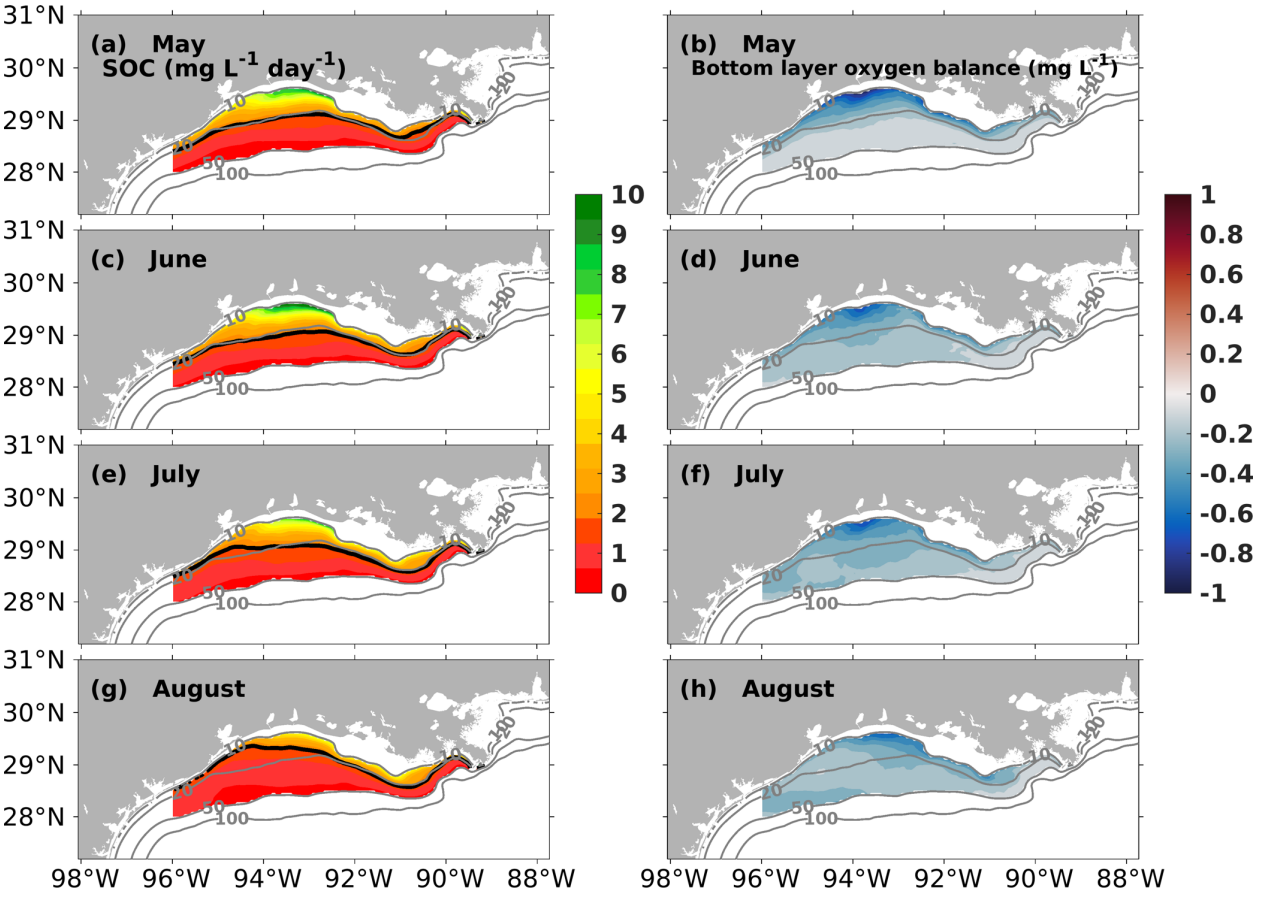

Figure 11. Spatial distribution of monthly climatology of sediment oxygen consumption (SOC, left panel) and DO balance at the bottom water layer (right panel). The black solid lines in the left panels indicate contour lines of 2 mg L^{-1} day^{-1}.

4.2.2 Stratification

Previous studies showed that water stratification regulates the oxygen replenishment and hypoxia dynamics in the LaTex Shelf (Hetland and DiMarco, 2008; Bianchi et al., 2010; Fennel et al., 2011, 2013, 2016; Justić and Wang, 2014; Wang and Justić, 2009; Feng et al., 2014; Yu et al., 2015; Laurent et al., 2018). Water column stratification measures the hydrodynamical stability of the column. When the stratification increases, surface oxygen (usually saturated due to oxygen supply by the atmosphere) is harder to penetrate down to fuel up the oxygen pool at the bottom layers. Potential energy anomaly (PEA in J m^{-3}) was obtained for quantifying water stratification according to

$$PEA = \frac{1}{H}\int_{-h}^{\eta}(\bar{\rho} - \rho)gzdz, \quad (12)$$

where ρ is water density profile over water column of depth $H = h + \eta$, h is the location of the bed, η is water surface elevation, g is the gravitational acceleration (9.8 m s^{-2}), z is the vertical axis, $\bar{\rho}$ is the depth-integrated water density given by $\bar{\rho} = \frac{1}{H}\int_{-h}^{\eta}\rho dz$ (Simpson and Hunter, 1974; Simpson et al., 1978; Simpson, 1981; Simpson and Bowers, 1981). Proposed by

https://doi.org/10.5194/bg-2022-3
Preprint. Discussion started: 11 January 2022

Simpson and Hunter (1974), PEA represents the amount of energy per volume to homogenize the entire water column. A greater PEA value represents a more stratified water column.

In nearshore regions, PEA increases from May to June (peak) followed by a salient decline in July and August (Figures 12a, 12c, 12e, and 12g). However, in the offshore regions, PEA increases steadily during summer. The spatial patterns of surface salinity and surface current velocity indicate that the evolution of PEA from May to August is highly related to the changes in river plume (Figures 12b, 12d, 12f, and 12h). In the mid- and west-Atchafalaya nearshore regions, current directions change from westward to northward in June through August. It results in high-saline water intrusions and downwelling in nearshore waters, which are favorable for a less stratified water column. However, in the west-Mississippi nearshore and offshore regions, dominant coastal current changes from strong westward flows in May and June to the weak westward and strong southward flows in July and August. Such a change in current direction leads to an offshore extension of low-saline surface water and strengthened water stratification. The extent of low-salinity water roughly outlines the shape of waters with high hypoxia frequency (Figure 9).

Daily climatology shows that PEA modulation on bottom DO concentration is more pronounced in the offshore regions where PEA increases dramatically (nearly 5-fold) in summer while SOC stabilizes around 1.5 mg L^{-1} day^{-1} over a year (Figure 10). Nevertheless, in mid- and west-Atchafalaya nearshore regions, PEA maintains lower than 100 J m^{-3} in summer, indicating the water column is less stratified, while SOC can reach up to 5 mg L^{-1} day^{-1}. The variability of bottom DO can be more affected by SOC over these nearshore regions. Influences of PEA and SOC seem to be comparable in the west-Mississippi nearshore region with salient increases found in both time series during summer.

https://doi.org/10.5194/bg-2022-3
Preprint. Discussion started: 11 January 2022

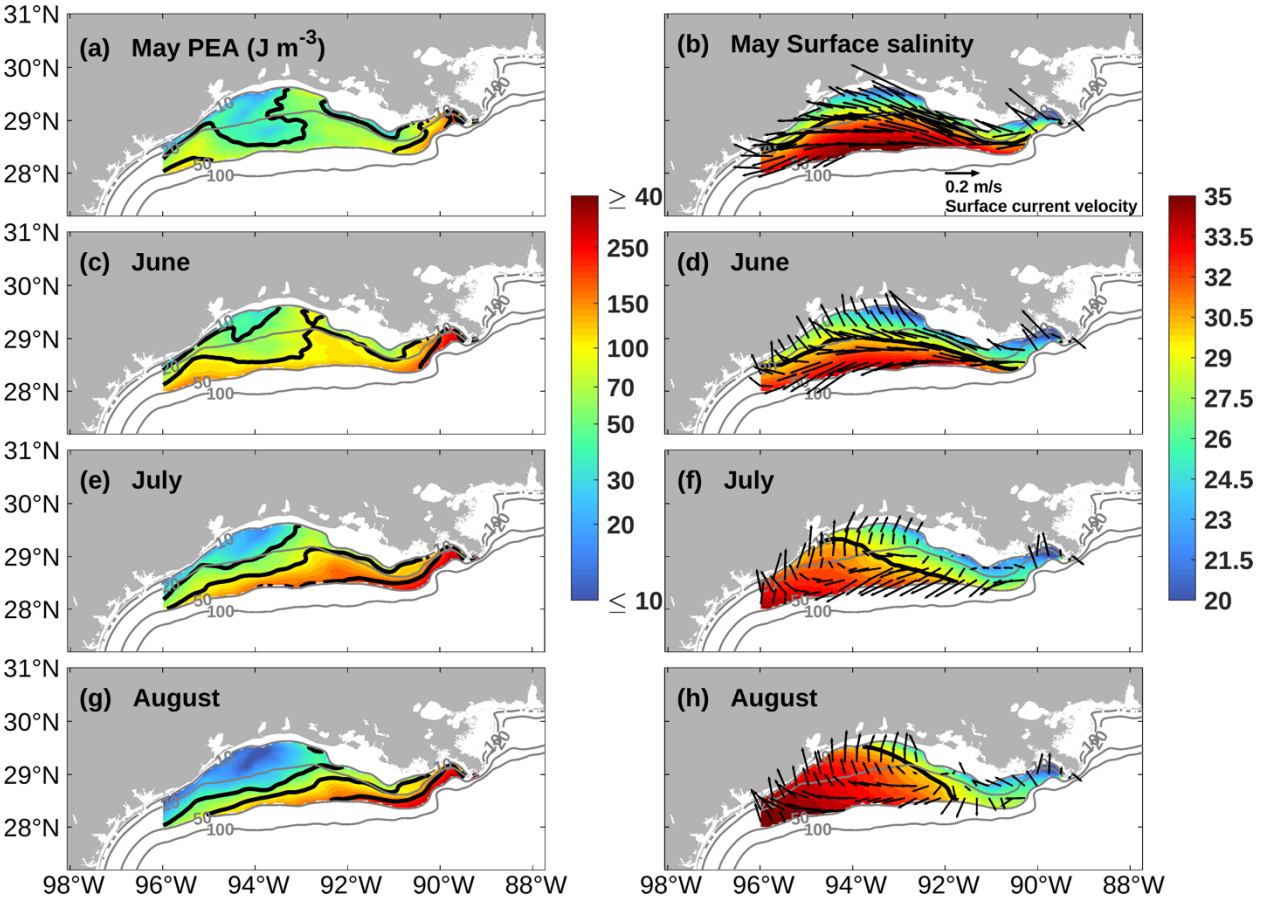

Figure 12. Spatial distribution of monthly climatology of potential energy anomaly (PEA, unit: J m^{-3}, left panel), surface salinity (color in the right panel), and surface current velocity (arrows in the right panel). Black solid lines in the left panel indicate PEA isolines of 50 J m^{-3}, 100 J m^{-3}, and 200 J m^{-3}, while those in the right panel denote isohaline of 30.

4.3 PEA and SOC's contribution to hypoxia development

The Generalized Boosted Regression Models (GBMs) available in an R package of "gbm" (version 2.1.8, Greenwell et al., 2020) were implemented to further quantify the contribution of PEA and SOC to bottom DO variability in different subregions. In machine learning, boosting is an ensemble algorithm to primarily reduce selected loss functions by iteratively adding basis functions in a greedy fashion. The implementation of package "gbm" closely follows Friedman's Gradient Boosting Machine (Friedman, 2001). The Laplace distribution was used since the response (i.e., regionally averaged bottom DO concentration) is left-skewed (figures not shown). The fraction of observations in the training set was set at 90 %, on which the GBMs were built. Half of the training set observations were randomly selected to build the next tree in the expansion (i.e., *bag.fraction*=0.5). The learning rate was 0.01 (i.e., *shrinkage*=0.01) which was set small to build more trees. The maximum tree depth or interactions order was set 6 considering regression trees with a complicated structure (i.e., *interaction.depth*=6).

https://doi.org/10.5194/bg-2022-3
Preprint. Discussion started: 11 January 2022

To find the optimal number of iterations, we performed a procedure as follows. (a) Build 1,000 trees by setting *n.trees*=1000. (b) Estimate the optimal number of iterations *best.iter* using function *gbm.perf* with the out-of-bag (OOB) method. (c) If *best.iter* found is within 50 to the number of iterations (here 1,000), then run 1,000 more iterations. Otherwise, stop. (d) Repeat steps (b) and (c) until the stopping criterion is met. We then estimated the relative importance of variable SOC and PEA using the sum of squared influence over the trees fitted (Friedman, 2001). The number of these fitted trees was *best.iter* found above.

We applied the GBMs to the hindcast daily time series (4,987 observations) of PEA (independent variable), SOC (independent variable), and bottom DO concentration (dependent variable) averaged over the 6 subregions, respectively. As shown in Figure 13, SOC is the primary modulator in nearshore regions with a percentage contribution ranging from 69 % to 83 %. The mid-Atchafalaya nearshore region has the greatest impact of SOC (83 %) on bottom DO variability. Accumulated sedimentary organic matter (figure not shown) is more abundant in this region where westward along-shore currents turn northward from June to August in favor of riverine nutrient accumulation. PEA becomes more important in offshore regions with a percentage contribution ranging from 66 % to 75 % emphasizing the importance of DO ventilation to bottom DO dynamics. However, as indicated in Figure 10, variability of bottom DO is generally weaker in the offshore regions, where hydrodynamics dominates the pattern, than in the nearshore regions, where the sedimentary biochemical process serves as the primary regulator. Results also indicate that the nearshore waters can be much more sensitive to the river nutrient reduction strategies than the offshore waters, which also suffer from massive hypoxia during mid and late summer. Influenced by the proceeding climate changes, the Mississippi River discharges would be substantially enhanced by 10.7–59.8 % by the 2090s (Tao et al., 2014). Accordingly, by the end of the 21st century, there would be remarkably increasing hypoxia events projected in the offshore region where water stratification is highly affected by the river freshwater supplies. However, more sensitivity studies are needed for quantifying the impacts of climate changes and nutrient reduction strategies on hypoxia in different shelf regions.

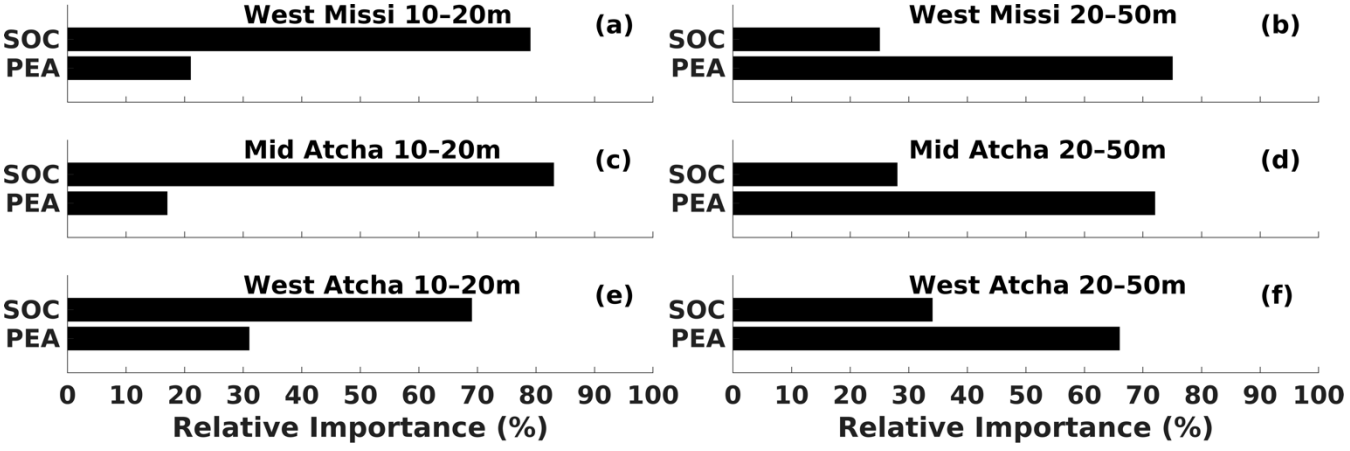

Figure 13. Relative importance of PEA and SOC on the variability of bottom DO concentration based on daily time series averaged over six subregions.

https://doi.org/10.5194/bg-2022-3
Preprint. Discussion started: 11 January 2022

531 **4.4 Factors to hypoxic volume variability**

532

533 Hypoxic volume in the LaTex Shelf was deemed to be more sensitive to the changes of river nitrogen loads than the hypoxic
534 area and was therefore considered as a more appropriate metric relevant to ecosystem-level effects (Scavia et al., 2019). We
535 estimated the hypoxic volume according to the thickness of hypoxia layers and the sizes of the corresponding grid cells. Over
536 the LaTex shelf (colored area in Figure 8d), the volume and area show a significant linear relationship ($r=0.94$, $p<0.001$),
537 especially when the area is low (Figure 14). However, a quadratic polynomial fitting curve is more representable and indicates
538 that their relationship changes as the area increases roughly beyond 20,000 km^2. Such a quadratic relationship was found very
539 closed to Scavia et al.'s (2019) analysis ($y=7E-8x^2+0.0028x$) although the maximum area in their study is about 25,000 km^2.
540 The nonlinear relationship found suggests that the bottom hypoxic condition can be important in regulating the hypoxia
541 evolution at non-bottom layers.

542

543 In our model, the settling velocity was set to 15 m day^{-1} for both PON and Opal (see Table B4). Thus, our biogeochemical
544 model parameterizes a fast-sinking system over the hypoxia-affected zone which has a maximum depth of about 50 m. Most
545 organic matter accumulates at the conceptual sediment layer instead of being recycled over the water column. As shown in
546 Figure 15, during summer, it is expected to have a much lower oxygen sink at water columns due to biochemical processes
547 than that at the conceptual sediment layer. Similar to the bottom DO seasonality, the depth-averaged DO seasonality is
548 regulated by SOC and water stratification rather than by the depth-averaged water column DO balances. During summer when
549 strong stratification encounters with high SOC, vertical DO gradients are thought to be increased enhancing the DO diffusion
550 from upper layers to lower layers. Hypoxic layers thus mostly extend from the water bottom as shown in both observed and
551 simulated DO profiles (Figure 4). Hypoxia thickness of 1–2 m is the most prevalent, although, it becomes thicker than 2 m and
552 even reaches up to 12 m at some locations (Figure 5). The above results indicate that the hypoxic volume mostly results from
553 the low bottom DO concentration due to the combined effects of stratification and sedimentary biochemical processes. The
554 strong significant relationship of the hypoxic volume and the hypoxic area provides us a possible way to predict the volume
555 according to the area alone in a fast and accurate manner.

https://doi.org/10.5194/bg-2022-3
Preprint. Discussion started: 11 January 2022

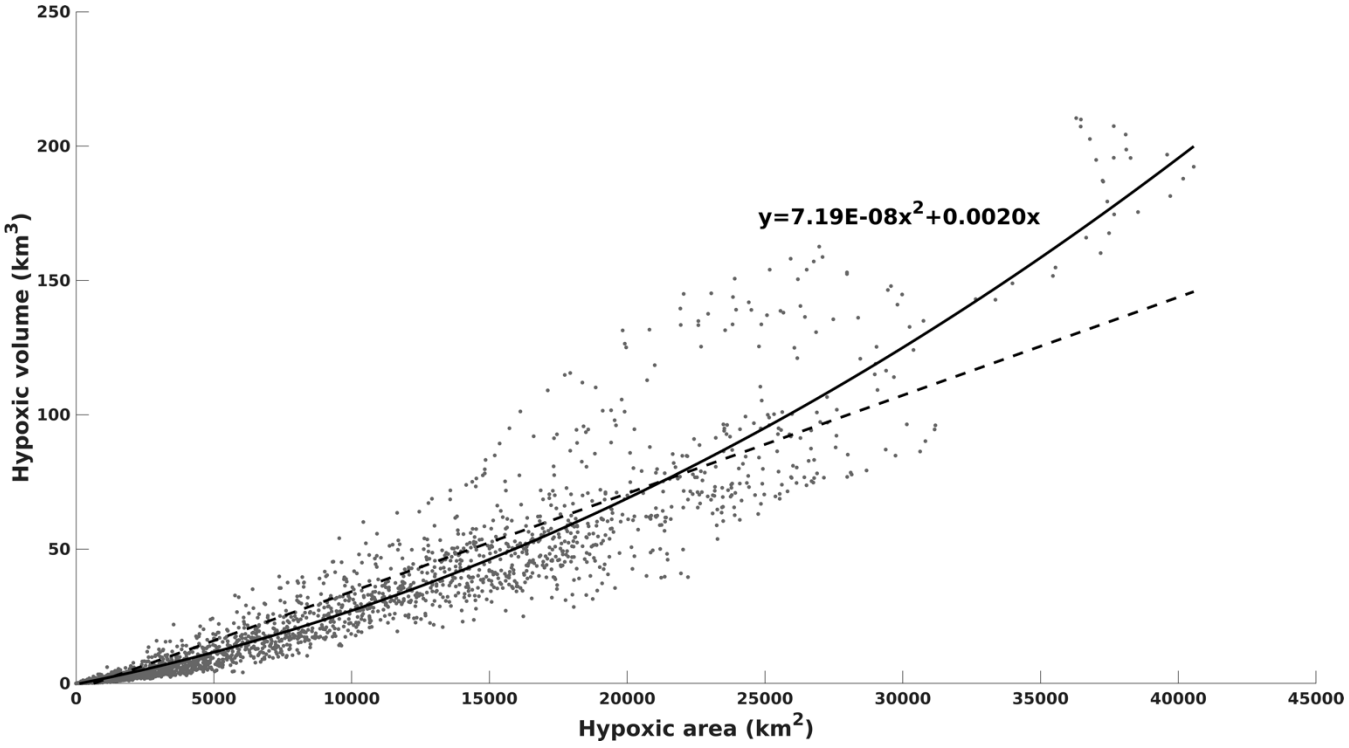

Figure 14. Scatter plots of hypoxic volume against hypoxic area, the corresponding linear fitting line (dashed line), and the quadratic polynomial fitting curve (solid line). Note that the expression shown describes the quadratic polynomial fitting curve.

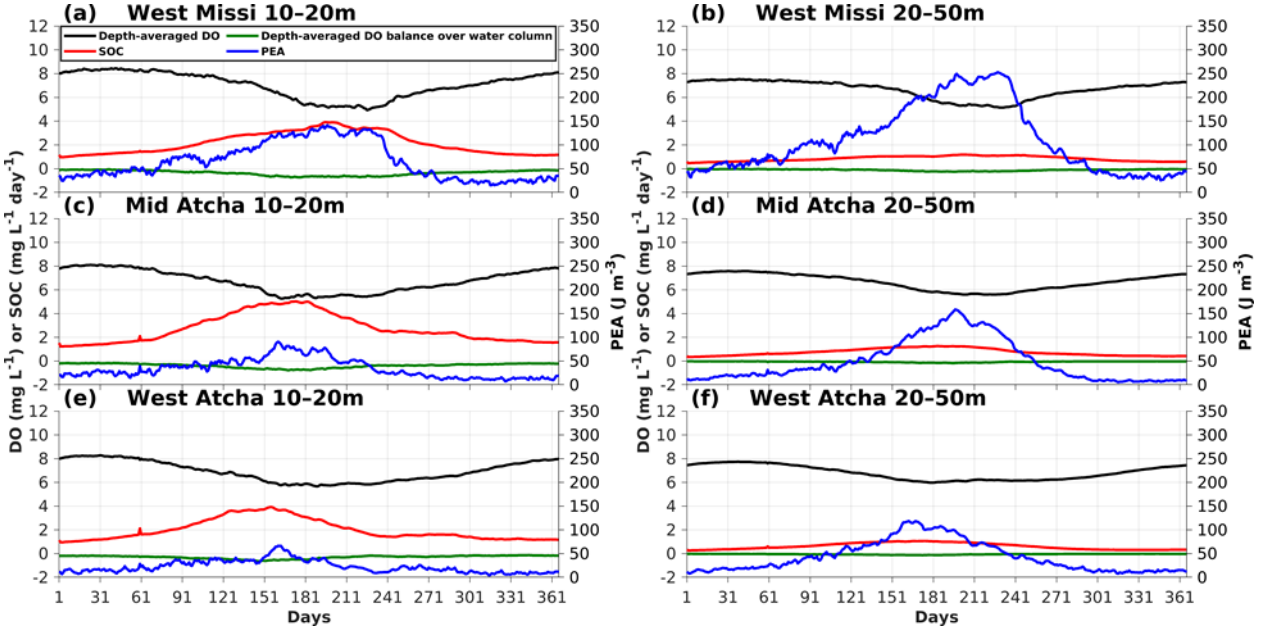

Figure 15. Time series of daily climatology (spatially averaged) of depth-averaged DO concentration, SOC, depth-averaged water column DO balance term, and PEA over the (a) west-Mississippi nearshore region, (b) west-Mississippi offshore region, (c) mid-Atchafalaya nearshore region, (d) mid-Atchafalaya offshore region, (e) west-Atchafalaya nearshore region, and (f) west-Atchafalaya

https://doi.org/10.5194/bg-2022-3
Preprint. Discussion started: 11 January 2022

563 **offshore region. Note that the water column DO balance term only accounts for the local biochemical processes at the corresponding**
564 **water layer.**

565 **5 Conclusions**

566

567 A three-dimensional coupled hydrodynamic–biogeochemical model was modified and applied to the Gulf of Mexico to study
568 bottom DO variability. The NEMURO was applied and modified since the model parameterizes a more sophisticated lower-
569 trophic ecosystem especially including a diatom functional group, which is the dominant species of the nGoM phytoplankton
570 community. An additional phosphorous flow was embedded into the NEMURO model to account for the impacts of
571 phosphorous limitation on hypoxia development. Built on the SOC scheme of the instantaneous remineralization developed
572 by Fennel et al. (2006), a pool of sedimentary PON was added to account for temporal delays in SOC to the peak of plankton
573 blooms. The model can well reproduce the vertical profiles of inorganic nutrient concentration (i.e., nitrate, phosphate, and
574 silicate). The model's robustness in DO simulation was affirmed via 1) comparison of the DO profiles against observations
575 from three different sets of cruises studies, 2) comparison of the frequency distribution of hypoxia thickness, spatial
576 distributions of bottom DO, and time series of hypoxic area against the Shelfwide cruises observations.
577

578 A 15 year model hindcast was achieved covering the period of 2006-2020. Multiyear mean, long-term trends, and STDs of
579 bottom DO concentration on the LaTex Shelf all highlight the impacts from two major river plumes (i.e., the Mississippi and
580 the Atchafalaya Rivers) and Louisiana coastal currents. May, June, July, and August are the months most affected by hypoxic
581 events (bottom DO concentration $\leq$ 2 mg L^{-1}). However, the developments of hypoxia are different in different subregions.
582 Based on the monthly climatology, the mid-Atchafalaya nearshore (10–20 m) region was first detected hypoxic in May while
583 hypoxic water was not found in the west-Mississippi nearshore region until June. The west hypoxic water expands offshore
584 and eastward in June and July and finally merges with the east hypoxic water in August.
585

586 The evolution of hypoxia in the LaTex Shelf (<50 m) is highly affected by SOC and water stratification (quantified by PEA).
587 Qualitative analysis suggests that their impacts on bottom DO vary in different shelf regimes. GBM analysis provides a
588 quantitative assessment of the relative importance of PEA and SOC on bottom DO variability in different subregions. SOC is
589 the main regulator in nearshore (10–20 m) regions while the PEA is the prevailing factor in the offshore (20–50 m) regions.
590 Nevertheless, the variability of bottom DO concentration is weaker in the hydrodynamic-dominated regions than in the regions
591 with stronger impacts of sedimentary biochemical processes. The hypoxic volume is significantly related to the hypoxic area
592 (r=0.94, p<0.001) which is mostly modulated by stratification and sedimentary biochemical processes. However, hypoxic
593 volume increases nonlinearly as the area reaches beyond 20,000 km^2 illustrating a quadratic relationship very close to the
594 previous relationship discovered by Scavia et al. (2019). Such results indicate that the hypoxic volume mostly resulting from
595 the low bottom DO concentration can be possibly predicted using the hypoxic area alone.
596

https://doi.org/10.5194/bg-2022-3
Preprint. Discussion started: 11 January 2022

597 **Code/Data availability:** Model data is available at the LSU mass storage system and details are on the webpage of the Coupled
598 Ocean Modeling Group at LSU (https://faculty.lsu.edu/zxue/). Data requests can be sent to the corresponding author via this
599 webpage.
600
601 **Author contribution:** Z. George Xue designed the experiments and Yanda Ou carried them out. Yanda Ou developed the
602 model code and performed the simulations. Yanda Ou and Z. George Xue prepared the manuscript.
603
604 **Competing interests:** The authors declare that they have no conflict of interest.
605
606 **Acknowledgment:** Research support was provided through the Bureau of Ocean Energy Management (M17AC00019,
607 M20AC10001). We thank Dr. Jerome Fiechter at UC Santa Cruz for sharing his NEMURO model codes. Computational
608 support was provided by the High-Performance Computing Facility (clusters SuperMIC and QueenBee3) at Louisiana State
609 University.
610
611

https://doi.org/10.5194/bg-2022-3
Preprint. Discussion started: 11 January 2022

Appendix A: Expressions of processes terms modified in this study

Detailed descriptions of related terms and parameters are listed in Appendix B.

A1 Update gross primary production of PS and PL due to the additional phosphate limitation

$$GppPSn = GppNPS + GppAPS, \quad (A1)$$

$$GppPLn = GppNPL + GppAPL, \quad (A2)$$

where,

$$GppNPS = PSn\, V_{maxS}\, exp\left(K_{GppS}\, TMP\right)\left[1 - exp\left(-\frac{\alpha_{PS}}{V_{maxS}} I_{PS}\right)\right] exp\left(-\frac{\beta_{PS}}{V_{maxS}} I_{PS}\right) NutlimPS\, RnewS, \quad (A3)$$

$$GppAPS = PSn\, V_{maxS}\, exp\left(K_{GppS}\, TMP\right)\left[1 - exp\left(-\frac{\alpha_{PS}}{V_{maxS}} I_{PS}\right)\right] exp\left(-\frac{\beta_{PS}}{V_{maxS}} I_{PS}\right) NutlimPS\, (1 - RnewS), \quad (A4)$$

$$GppNPL = PLn\, V_{maxL}\, exp\left(K_{GppL}\, TMP\right)\left[1 - exp\left(-\frac{\alpha_{PL}}{V_{maxL}} I_{PL}\right)\right] exp\left(-\frac{\beta_{PL}}{V_{maxL}} I_{PL}\right) NutlimPL\, RnewL, \quad (A5)$$

$$GppAPL = PLn\, V_{maxL}\, exp\left(K_{GppL}\, TMP\right)\left[1 - exp\left(-\frac{\alpha_{PL}}{V_{maxL}} I_{PL}\right)\right] exp\left(-\frac{\beta_{PL}}{V_{maxL}} I_{PL}\right) NutlimPL\, (1 - RnewL), \quad (A6)$$

$$RnewS = \frac{\frac{NO_3}{\left(NO_3 + K_{NO_3S}\right)\left(1 + \frac{NH_4}{K_{NH_4S}}\right)}}{\frac{NO_3}{\left(NO_3 + K_{NO_3S}\right)\left(1 + \frac{NH_4}{K_{NH_4S}}\right)} + \frac{NH_4}{NH_4 + K_{NH_4S}}}, \quad (A7)$$

$$RnewL = \frac{\frac{NO_3}{\left(NO_3 + K_{NO_3L}\right)\left(1 + \frac{NH_4}{K_{NH_4L}}\right)}}{\frac{NO_3}{\left(NO_3 + K_{NO_3L}\right)\left(1 + \frac{NH_4}{K_{NH_4L}}\right)} + \frac{NH_4}{NH_4 + K_{NH_4L}}}, \quad (A8)$$

$$NutlimPS = min\left(\frac{NO_3}{\left(NO_3 + K_{NO_3S}\right)\left(1 + \frac{NH_4}{K_{NH_4S}}\right)} + \frac{NH_4}{NH_4 + K_{NH_4S}}, \frac{PO_4}{PO_4 + K_{PO_4S}}\right), \quad (A9)$$

$$NutlimPL = min\left(\frac{NO_3}{\left(NO_3 + K_{NO_3L}\right)\left(1 + \frac{NH_4}{K_{NH_4L}}\right)} + \frac{NH_4}{NH_4 + K_{NH_4L}}, \frac{PO_4}{PO_4 + K_{PO_4L}}, \frac{SiOH_4}{SiOH_4 + K_{SiOH_4L}}\right), \quad (A10)$$

$$I_{PS} = PAR\, frac\, exp\left\{z\, AttSW + AttPS \int_z^0 [PSn(\zeta) + PLn(\zeta)] d\zeta\right\}, \quad (A11)$$

$$I_{PL} = PAR\, frac\, exp\left\{z\, AttSW + AttPL \int_z^0 [PSn(\zeta) + PLn(\zeta)] d\zeta\right\}, \quad (A12)$$

A2 Update aerobic decomposition from PON to NH_4 and from DON to NH_4 due to introduction of oxygen dependency

$$DecP2N = PON\, VP2N_0\, exp(K_{P2N}\, TMP)\, \hat{r}, \quad (A13)$$

$$DecD2N = PON\, VD2N_0\, exp(K_{D2N}\, TMP)\, \hat{r}, \quad (A14)$$

where,

$$\hat{r} = max\left[\frac{max(0, Oxyg - Oxyg_{th})}{K_{Oxyg} + Oxyg - Oxyg_{th}}, 0\right], \quad (A15)$$

https://doi.org/10.5194/bg-2022-3
Preprint. Discussion started: 11 January 2022

A3 Update water column nitrification due to introduction of oxygen dependency and light limitation

$$Nit = Nit_0 exp(K_{Nit}\, TMP)\; LgtlimN\; \hat{r}, \tag{A16}$$

where,

$$LgtlimN = 1 - max\left(0, \frac{I_N - I_0}{I_N - I_0 + k_I}\right), \tag{A17}$$

$$I_N = PAR\; frac\; exp\left\{z\; AttSW + max(AttPS, AttPL) \int_z^0 [PSn(\zeta) + PLn(\zeta)] d\zeta\right\}, \tag{A18}$$

A4 Additional SOC term:

$$SOC = 8.3865\; PON_{sed}\; VP2N_0\; exp(K_{P2N}\, TMP), \tag{A19}$$

Appendix B: Descriptions of terms and parameters

Table B1. Descriptions of state variables

Terms	Description	Unit
NH_4	Ammonium concentration	mmolN m^{-3}
NO_3	Nitrate concentration	mmolN m^{-3}
PO_4	Phosphate concentration	mmolP m^{-3}
DOP	Dissolved organic phosphorous concentration	mmolP m^{-3}
POP	Particulate organic phosphorous concentration	mmolP m^{-3}
$SiOH_4$	Silicate concentration	mmolSi m^{-3}
PSn	Small phytoplankton biomass concentration measured in nitrogen	mmolN m^{-3}
PLn	Large phytoplankton biomass concentration measured in nitrogen	mmolN m^{-3}
$Oxyg$	Dissolved oxygen concentration	mmolO_2 m^{-3}

Table B2 Descriptions of related terms involved in the phosphorus cycle and nutrient limitation. Superscript "*" and "+" denote that the mathematic expressions of corresponding terms are the same as those in Kishi et al. (2007) and Shropshire et al. (2020), respectively. Expressions of terms with no superscript are updated and reported in Appendix A.

Terms	Description	Unit
$DecP2N$	Decomposition rate from PON to NH_4	mmolN m^{-3} day^{-1}
$DecD2N$	Decomposition rate from DON to NH_4	mmolN m^{-3} day^{-1}
$DecP2D^{*+}$	Decomposition rate from PON to DON	mmolN m^{-3} day^{-1}
$EgeZLn^{+}$	Large zooplankton egestion rate measured in nitrogen	mmolN m^{-3} day^{-1}
$EgeZPn^{*+}$	Predatory zooplankton egestion rate measured in nitrogen	mmolN m^{-3} day^{-1}

https://doi.org/10.5194/bg-2022-3
Preprint. Discussion started: 11 January 2022


Biogeosciences Discussions Open Access EGU

$EgeZSn^{*+}$	Small zooplankton egestion rate measured in nitrogen	mmolN m^{-3} day^{-1}
$ExcPSn^{*+}$	Small phytoplankton extracellular excretion rate to DON and is measured in nitrogen	mmolN m^{-3} day^{-1}
$ExcPLn^{*+}$	Large phytoplankton extracellular excretion rate to DON and is measured in nitrogen	mmolN m^{-3} day^{-1}
$ExcZSn^{*+}$	Small zooplankton excretion rate to NH_4 and is measured in nitrogen	mmolN m^{-3} day^{-1}
$ExcZLn^{+}$	Large zooplankton excretion rate to NH_4 and is measured in nitrogen	mmolN m^{-3} day^{-1}
$ExcZPn^{*+}$	Predatory zooplankton excretion rate to NH_4 and is measured in nitrogen	mmolN m^{-3} day^{-1}
$GppNPS$	Small phytoplankton nitrate-induced gross primary production rate measured in nitrogen	mmolN m^{-3} day^{-1}
$GppAPS$	Small phytoplankton ammonium-induced gross primary production rate measured in nitrogen	mmolN m^{-3} day^{-1}
$GppPSn$	Small phytoplankton gross primary production rate measured in nitrogen	mmolN m^{-3} day^{-1}
$GppNPL$	Large phytoplankton nitrate-induced gross primary production rate measured in nitrogen	mmolN m^{-3} day^{-1}
$GppAPL$	Large phytoplankton ammonium-induced gross primary production rate measured in nitrogen	mmolN m^{-3} day^{-1}
$GppPLn$	Large phytoplankton gross primary production rate measured in nitrogen	mmolN m^{-3} day^{-1}
$MorPSn^{+}$	Small phytoplankton mortality rate measured in nitrogen	mmolN m^{-3} day^{-1}
$MorPLn^{+}$	Large phytoplankton mortality rate measured in nitrogen	mmolN m^{-3} day^{-1}
$MorZSn^{+}$	Small zooplankton mortality rate measured in nitrogen	mmolN m^{-3} day^{-1}
$MorZLn^{+}$	Large zooplankton mortality rate measured in nitrogen	mmolN m^{-3} day^{-1}
$MorZPn^{*+}$	Predatory zooplankton mortality rate measured in nitrogen	mmolN m^{-3} day^{-1}
Nit	Nitrification rate	mmolN m^{-3} day^{-1}
$ResPSn^{*+}$	Small phytoplankton respiration rate measured in nitrogen	mmolN m^{-3} day^{-1}
$ResPLn^{*+}$	Large phytoplankton respiration rate measured in nitrogen	mmolN m^{-3} day^{-1}
SOC	Sediment oxygen consumption rate	mmolO_2 m^{-2} day^{-1}

Table B3 Descriptions of other variables

https://doi.org/10.5194/bg-2022-3
Preprint. Discussion started: 11 January 2022

Terms	Description	Unit
I_{PS}	Photosynthetically available radiation for small phytoplankton	W m^{-2}
I_{PL}	Photosynthetically available radiation for large phytoplankton	W m^{-2}
I_N	Maximum photosynthetically available radiation	W m^{-2}
$LgtlimN$	Light inhibition on nitrification rate	no dimension
$NutlimPS$	Nutrient limitation term for small phytoplankton	no dimension
$NutlimPL$	Nutrient limitation term for large phytoplankton	no dimension
PAR	Net short-wave radiation on water surface	W m^{-2}
$\hat{r}$	Oxygen inhibition on nitrification and aerobic decomposition rates	no dimension
$RnewS$	The f-ratio of small phytoplankton which is defined by the ratio of nitrate uptake to total uptake of nitrate and ammonium	no dimension
$RnewL$	The f-ratio of large phytoplankton which is defined by the ratio of nitrate uptake to total uptake of nitrate and ammonium	no dimension
$Thickness_{bot}$	Thickness of the bottom water layer	m
TMP	Water temperature	°C
z, ζ	Vertical coordinate which is negative below sea surface	m

Table B4. Descriptions and values of all model parameters

Parameter	Description	Units	Values
	Small phytoplankton		
V_{maxS}	Small phytoplankton maximum photosynthetic rate at 0 ℃	day^{-1}	0.4
K_{NO_3S}	Small Phytoplankton half saturation constant for nitrate	mmolN m^{-3}	0.5
K_{NH_4S}	Small Phytoplankton half saturation constant for ammonium	mmolN m^{-3}	0.1
K_{PO_4S}	Small Phytoplankton half saturation constant for phosphate	mmolP m^{-3}	0.5
α_{PS}	Small phytoplankton photochemical reaction coefficient, initial slope of P-I curve	m^2 W^{-1} day^{-1}	0.1
β_{PS}	Small phytoplankton photoinhibition coefficient	m^2 W^{-1} day^{-1}	0.00045

https://doi.org/10.5194/bg-2022-3
Preprint. Discussion started: 11 January 2022

Res_{PS0}	Small phytoplankton respiration rate at 0 ℃	day^{-1}	0.03
Mor_{PS0}	Small phytoplankton mortality rate at 0 ℃	m^3 mmolN^{-1} day^{-1}	0.002
γ_S	Ratio of extracellular excretion to photosynthesis for small phytoplankton	no dimension	0.135
K_{GppS}	Small phytoplankton temperature coefficient for photosynthetic rate	$℃^{-1}$	0.0693
K_{ResPS}	Small phytoplankton temperature coefficient for respiration	$℃^{-1}$	0.0519
K_{MorPS}	Small phytoplankton temperature coefficient for mortality	$℃^{-1}$	0.0693
	Large phytoplankton		
V_{maxL}	Large phytoplankton maximum photosynthetic rate at 0 ℃	day^{-1}	0.8
K_{NO_3L}	Large Phytoplankton half saturation constant for nitrate	mmolN m^{-3}	3.0
K_{NH_4L}	Large Phytoplankton half saturation constant for ammonium	mmolN m^{-3}	0.3
K_{PO_4L}	Large Phytoplankton half saturation constant for phosphate	mmolP m^{-3}	0.5
K_{SiOH_4L}	Large Phytoplankton half saturation constant for silicate	mmolSi m^{-3}	6.0
α_{PL}	Large phytoplankton photochemical reaction coefficient, initial slope of P-I curve	m^2 W^{-1} day^{-1}	0.1
β_{PL}	Large phytoplankton photoinhibition coefficient	m^2 W^{-1} day^{-1}	0.00045
Res_{PL0}	Large phytoplankton respiration rate at 0 ℃	day^{-1}	0.03
Mor_{PL0}	Large phytoplankton mortality rate at 0 ℃	m^3 mmolN^{-1} day^{-1}	0.001
γ_L	Ratio of extracellular excretion to photosynthesis for large phytoplankton	no dimension	0.135

https://doi.org/10.5194/bg-2022-3
Preprint. Discussion started: 11 January 2022

K_{GppL}	Large phytoplankton temperature coefficient for photosynthetic rate	$℃^{-1}$	0.0693
K_{MorPL}	Large phytoplankton temperature coefficient for mortality	$℃^{-1}$	0.0693
K_{ResPL}	Large phytoplankton temperature coefficient for respiration	$℃^{-1}$	0.0693
	Small zooplankton		
GR_{maxSps}	Small zooplankton maximum grazing rate on small phytoplankton at 0 ℃	day^{-1}	0.6
λ_S	Ivlev constant of small zooplankton	$m^3\ mmolN^{-1}$	1.4
$PS2ZS$	Small zooplankton threshold value for grazing on small phytoplankton	$mmolN\ m^{-3}$	0.043
α_{ZS}	Assimilation efficiency of small zooplankton	no dimension	0.7
β_{ZS}	Growth efficiency of small zooplankton	no dimension	0.3
Mor_{ZS0}	Small zooplankton mortality rate at 0 ℃	$m^3\ mmolN^{-1}\ day^{-1}$	0.022
K_{GraS}	Small zooplankton temperature coefficient for grazing	$℃^{-1}$	0.0693
K_{MorZS}	Small zooplankton temperature coefficient for mortality	$℃^{-1}$	0.0693
	Large zooplankton		
GR_{maxLps}	Large zooplankton maximum grazing rate on small phytoplankton at 0 ℃	day^{-1}	0
GR_{maxLpl}	Large zooplankton maximum grazing rate on large phytoplankton at 0 ℃	day^{-1}	0.3
GR_{maxLzs}	Large zooplankton maximum grazing rate on small zooplankton at 0 ℃	day^{-1}	0.3
λ_L	Ivlev constant of large zooplankton	$m^3\ mmolN^{-1}$	1.4
$PL2ZL$	Large zooplankton threshold value for grazing on large phytoplankton	$mmolN\ m^{-3}$	0.040
$ZS2ZL$	Large zooplankton threshold value for grazing on small zooplankton	$mmolN\ m^{-3}$	0.040

https://doi.org/10.5194/bg-2022-3
Preprint. Discussion started: 11 January 2022

α_{ZL}	Assimilation efficiency of large zooplankton	no dimension	0.7
β_{ZL}	Growth efficiency of large zooplankton	no dimension	0.3
Mor_{ZL0}	Large zooplankton mortality rate at 0 ℃	m^3 $mmolN^{-1}$ day^{-1}	0.022
K_{GraL}	Large zooplankton temperature coefficient for grazing	$℃^{-1}$	0.0693
K_{MorZL}	Large zooplankton temperature coefficient for mortality	$℃^{-1}$	0.0693
	Predatory zooplankton		
GR_{maxPpl}	Predatory zooplankton maximum grazing rate on large phytoplankton at 0 ℃	day^{-1}	0.1
GR_{maxPzs}	Predatory zooplankton maximum grazing rate on small zooplankton at 0 ℃	day^{-1}	0.1
GR_{maxPzl}	Predatory zooplankton maximum grazing rate on large zooplankton at 0 ℃	day^{-1}	0.3
λ_P	Ivlev constant of predatory zooplankton	m^3 $mmolN^{-1}$	1.4
$PL2ZP$	Predatory zooplankton threshold value for grazing on large phytoplankton	mmolN m^{-3}	0.040
$ZS2ZP$	Predatory zooplankton threshold value for grazing on small zooplankton	mmolN m^{-3}	0.040
$ZL2ZP$	Predatory zooplankton threshold value for grazing on large zooplankton	mmolN m^{-3}	0.040
α_{ZP}	Assimilation efficiency of predatory zooplankton	no dimension	0.7
β_{ZP}	Growth efficiency of predatory zooplankton	no dimension	0.3
Mor_{ZP0}	Predatory zooplankton mortality rate at 0 ℃	m^3 $mmolN^{-1}$ day^{-1}	0.12
K_{GraP}	Predatory zooplankton temperature coefficient for grazing	$℃^{-1}$	0.0693
K_{MorZP}	Predatory zooplankton temperature coefficient for mortality	$℃^{-1}$	0.0693

https://doi.org/10.5194/bg-2022-3
Preprint. Discussion started: 11 January 2022

ψ_{PL}	Grazing inhibition coefficient of predatory zooplankton grazing on large phytoplankton	m^3 $mmolN^{-1}$	4.605
ψ_{ZS}	Grazing inhibition coefficient of predatory zooplankton grazing on small zooplankton	m^3 $mmolN^{-1}$	3.01
	Light		
$AttSW$	Light attenuation due to seawater	m^{-1}	0.03
$AttPS$	Light attenuation due to small phytoplankton, self-shading coefficient	m^2 $mmolN^{-1}$	0.03
$AttPL$	Light attenuation due to large phytoplankton, self-shading coefficient	m^2 $mmolN^{-1}$	0.03
$frac$	Fraction of shortwave radiation that is photosynthetically active	no dimension	0.43
I_0	Threshold of light inhibition of nitrification	W m^{-2}	0.0095
k_I	Light intensity at which light inhibition of nitrification is half-saturated	W m^{-2}	0.1
	Water column nitrification and aerobic decomposition		
Nit_0	Nitrification rate at 0 ℃	day^{-1}	0.003
$VP2N_0$	Decomposition rate at 0 ℃ (PON→NH_4)	day^{-1}	0.01
$VP2D_0$	Decomposition rate at 0 ℃ (PON→DON)	day^{-1}	0.05
$VD2N_0$	Decomposition rate at 0 ℃ (DON→NH_4)	day^{-1}	0.02
$VO2S_0$	Decomposition rate at 0 ℃ (Opal→$Si(OH)_4$)	day^{-1}	0.01
K_{Nit}	Temperature coefficient for nitrification	$℃^{-1}$	0.0693
K_{P2D}	Temperature coefficient for decomposition (PON→DON)	$℃^{-1}$	0.0693
K_{P2N}	Temperature coefficient for decomposition (PON→NH_4)	$℃^{-1}$	0.0693
K_{D2N}	Temperature coefficient for decomposition (DON→NH_4)	$℃^{-1}$	0.0693
K_{O2S}	Temperature coefficient for decomposition (Opal→$Si(OH)_4$)	$℃^{-1}$	0.0693

https://doi.org/10.5194/bg-2022-3
Preprint. Discussion started: 11 January 2022

Other parameters			
K_{Oxyg}	Oxygen concentration at which inhibition of nitrification and aerobic respiration are half-saturated	$mmolO_2\ m^{-3}$	3.0
$Oxyg_{th}$	Oxygen concentration threshold below which no aerobic respiration or nitrification occurs	$mmolO_2\ m^{-3}$	6.0
$RPO4N$	P: N ratio	$mmolP\ mmolN^{-1}$	1/16
$RSiN$	Si: N ratio	$mmolSi\ mmolN^{-1}$	1
$rOxNO_3$	Stoichiometric ratios corresponding to the oxygen produced per mol of nitrate assimilated during photosynthesis	$mmolO_2\ mmolNO_3^{-1}$	138/16
$rOxNH_4$	Stoichiometric ratios corresponding to the oxygen produced per mol of ammonium assimilated during photosynthesis	$mmolO_2\ mmolNH_4^{-1}$	106/16
$setVPON$	Sinking velocity of PON	$m\ day^{-1}$	-15
$setVOpal$	Sinking velocity of Opal	$m\ day^{-1}$	-15

References

Anglès, S., Jordi, A., Henrichs, D. W., and Campbell, L.: Influence of coastal upwelling and river discharge on the phytoplankton community composition in the northwestern Gulf of Mexico, Prog. Oceanogr., 173, 26–36, https://doi.org/10.1016/j.pocean.2019.02.001, 2019.

Bianchi, T. S., DiMarco, S. F., Cowan, J. H., Hetland, R. D., Chapman, P., Day, J. W., and Allison, M. A.: The science of hypoxia in the northern Gulf of Mexico: A review, Sci. Total Environ., 408, 1471–1484, https://doi.org/10.1016/j.scitotenv.2009.11.047, 2010.

Boyer, T. P., Baranova, O. K., Coleman, C., Garcia, H. E., Grodsky, A., Locarnini, R. A., Mishonov, A. V, Paver, C. R., Reagan, J. R., Seidov, D., Smolyar, I. V, Weathers, K. W., and Zweng, M. M.: World Ocean Database 2018, Technical., edited by: Mishonov, A. V., NOAA Atlas NESDIS 87, 2018.

Chakraborty, S. and Lohrenz, S. E.: Phytoplankton community structure in the river-influenced continental margin of the northern Gulf of Mexico, Mar. Ecol. Prog. Ser., 521, 31–47, https://doi.org/10.3354/meps11107, 2015.

Chakraborty, S., Lohrenz, S. E., and Gundersen, K.: Photophysiological and light absorption properties of phytoplankton communities in the river-dominated margin of the northern Gulf of Mexico, J. Geophys. Res. Ocean., 122, 4922–4938, https://doi.org/10.1002/2016JC012092, 2017.

Chapman, D. C.: Numerical treatment of cross-shelf open boundaries in a barotropic coastal ocean model, J. Phys. Oceanogr., 15, 1060–1075, https://doi.org/10.1175/1520-0485(1985)015<1060:ntocso>2.0.co;2, 1985.

Conley, D. J., Paerl, H. W., Howarth, R. W., Boesch, D. F., Seitzinger, S. P., Havens, K. E., Lancelot, C., and Likens, G. E.: Controlling

668 Eutrophication: Nitrogen and Phosphorus, Science, 323, 1014–1015, https://doi.org/10.1126/science.1167755, 2009.

669 Cummings, J. A.: Operational multivariate ocean data assimilation, Q. J. R. Meteorol. Soc., 131, 3583–3604,
670 https://doi.org/10.1256/qj.05.105, 2005.

671 Cummings, J. A. and Smedstad, O. M.: Variational Data Assimilation for the Global Ocean, in: Data Assimilation for Atmospheric, Oceanic
672 and Hydrologic Applications, vol. II, edited by: Park, S. K. and Xu, L., Springer Berlin Heidelberg, 303–343, https://doi.org/10.1007/978-
673 3-642-35088-7_13, 2013.

674 Feng, Y., Fennel, K., Jackson, G. A., DiMarco, S. F., and Hetland, R. D.: A model study of the response of hypoxia to upwelling-favorable
675 wind on the northern Gulf of Mexico shelf, J. Mar. Syst., 131, 63–73, https://doi.org/10.1016/j.jmarsys.2013.11.009, 2014.

676 Fennel, K. and Laurent, A.: N and P as ultimate and proximate limiting nutrients in the northern Gulf of Mexico: Implications for hypoxia
677 reduction strategies, Biogeosciences, 15, 3121–3131, https://doi.org/10.5194/bg-15-3121-2018, 2018.

678 Fennel, K. and Testa, J. M.: Biogeochemical Controls on Coastal Hypoxia, Ann. Rev. Mar. Sci., 11, 105–130,
679 https://doi.org/10.1146/annurev-marine-010318-095138, 2019.

680 Fennel, K., Wilkin, J., Levin, J., Moisan, J., O'Reilly, J., and Haidvogel, D.: Nitrogen cycling in the Middle Atlantic Bight: Results from a
681 three-dimensional model and implications for the North Atlantic nitrogen budget, Global Biogeochem. Cycles, 20, 1–14,
682 https://doi.org/10.1029/2005GB002456, 2006.

683 Fennel, K., Hetland, R., Feng, Y., and Dimarco, S.: A coupled physical-biological model of the Northern Gulf of Mexico shelf: Model
684 description, validation and analysis of phytoplankton variability, Biogeosciences, 8, 1881–1899, https://doi.org/10.5194/bg-8-1881-2011,
685 2011.

686 Fennel, K., Hu, J., Laurent, A., Marta-Almeida, M., and Hetland, R.: Sensitivity of hypoxia predictions for the northern Gulf of Mexico to
687 sediment oxygen consumption and model nesting, J. Geophys. Res. Ocean., 118, 990–1002, https://doi.org/10.1002/jgrc.20077, 2013.

688 Fennel, K., Laurent, A., Hetland, R., Justic, D., Ko, D. S., Lehrter, J., Murrell, M., Wang, L., Yu, L., and Zhang, W.: Effects of model physics
689 on hypoxia simulations for the northern Gulf of Mexico: A model intercomparison, J. Geophys. Res. Ocean., 121, 5731–5750,
690 https://doi.org/10.1002/2015JC011516, 2016.

691 Fiechter, J. and Moore, A. M.: Interannual spring bloom variability and Ekman pumping in the coastal Gulf of Alaska, J. Geophys. Res.
692 Ocean., 114, 1–19, https://doi.org/10.1029/2008JC005140, 2009.

693 Flather, R. A.: A tidal model of the northwest European continental shelf, Mem. la Soc. R. Sci. Liege, 6, 141–164, 1976.

694 Fox, D. N., Teague, W. J., Barron, C. N., Carnes, M. R., and Lee, C. M.: The Modular Ocean Data Assimilation System (MODAS), J.
695 Atmos. Ocean. Technol., 19, 240–252, https://doi.org/10.1175/1520-0426(2002)019<0240:TMODAS>2.0.CO;2, 2002.

696 Friedman, J. H.: Greedy function approximation: A gradient boosting machine, Ann. Stat., 29, 1189–1232,
697 https://doi.org/10.1214/aos/1013203451, 2001.

698 Garcia, H. E., Weathers, K., Paver, C. R., Smolyar, I., Boyer, T. P., Locarnini, R. A., Zweng, M. M., Mishonov, A. V., Baranova, O. K.,
699 Seidov, D., and Reagan, J. R.: World Ocean Atlas 2018, Volume 3: Dissolved Oxygen, Apparent Oxygen Utilization, and Oxygen Saturation,
700 Technical., edited by: Mishonov, A. V., NOAA Atlas NESDIS 83, 38 pp., 2018.

701 Gomez, F. A., Lee, S.-K., Liu, Y., Hernandez, F. J., Muller-Karger, F. E., and Lamkin, J. T.: Seasonal patterns in phytoplankton biomass
702 across the northern and deep Gulf of Mexico: A numerical model study, Biogeosciences, 15, 1–34, https://doi.org/10.5194/bg-15-3561-2018,
703 2018.

704 Greenwell, B., Boehmke, B., Cunningham, J., and Developers, G.: gbm: Generalized boosted regression models, https://github.com/gbm-
705 developers/gbm, 2020.

706 Große, F., Fennel, K., and Laurent, A.: Quantifying the Relative Importance of Riverine and Open-Ocean Nitrogen Sources for Hypoxia
707 Formation in the Northern Gulf of Mexico, J. Geophys. Res. Ocean., 5451–5467, https://doi.org/10.1029/2019jc015230, 2019.

Haidvogel, D. B., Arango, H. G., Hedstrom, K., Beckmann, A., Malanotte-Rizzoli, P., and Shchepetkin, A. F.: Model evaluation experiments in the North Atlantic Basin: Simulations in nonlinear terrain-following coordinates, Dyn. Atmos. Ocean., 32, 239–281, https://doi.org/10.1016/S0377-0265(00)00049-X, 2000.

Helber, R. W., Townsend, T. L., Barron, C. N., Dastugue, J. M., and Carnes, M. R.: Validation Test Report for the Improved Synthetic Ocean Profile (ISOP) System, Part I: Synthetic Profile Methods and Algorithm, 2013.

Hetland, R. D. and DiMarco, S. F.: How does the character of oxygen demand control the structure of hypoxia on the Texas-Louisiana continental shelf?, J. Mar. Syst., 70, 49–62, https://doi.org/10.1016/j.jmarsys.2007.03.002, 2008.

Justić, D. and Wang, L.: Assessing temporal and spatial variability of hypoxia over the inner Louisiana-upper Texas shelf: Application of an unstructured-grid three-dimensional coupled hydrodynamic-water quality model, Cont. Shelf Res., 72, 163–179, https://doi.org/10.1016/j.csr.2013.08.006, 2014.

Kishi, M. J., Kashiwai, M., Ware, D. M., Megrey, B. A., Eslinger, D. L., Werner, F. E., Noguchi-Aita, M., Azumaya, T., Fujii, M., Hashimoto, S., Huang, D., Iizumi, H., Ishida, Y., Kang, S., Kantakov, G. A., Kim, H. cheol, Komatsu, K., Navrotsky, V. V., Smith, S. L., Tadokoro, K., Tsuda, A., Yamamura, O., Yamanaka, Y., Yokouchi, K., Yoshie, N., Zhang, J., Zuenko, Y. I., and Zvalinsky, V. I.: NEMURO-a lower trophic level model for the North Pacific marine ecosystem, Ecol. Modell., 202, 12–25, https://doi.org/10.1016/j.ecolmodel.2006.08.021, 2007.

Laurent, A. and Fennel, K.: Simulated reduction of hypoxia in the northern Gulf of Mexico due to phosphorus limitation, Elementa: Science of the Anthropocene, 2, 1–12, https://doi.org/10.12952/journal.elementa.000022, 2014.

Laurent, A., Fennel, K., Hu, J., and Hetland, R.: Simulating the effects of phosphorus limitation in the Mississippi and Atchafalaya river plumes, Biogeosciences, 9, 4707–4723, https://doi.org/10.5194/bg-9-4707-2012, 2012.

Laurent, A., Fennel, K., Wilson, R., Lehrter, J., and Devereux, R.: Parameterization of biogeochemical sediment-water fluxes using in situ measurements and a diagenetic model, 13, 77–94, https://doi.org/10.5194/bg-13-77-2016, 2016.

Laurent, A., Fennel, K., Ko, D. S., and Lehrter, J.: Climate change projected to exacerbate impacts of coastal Eutrophication in the Northern Gulf of Mexico, J. Geophys. Res. Ocean., 123, 3408–3426, https://doi.org/10.1002/2017JC013583, 2018.

Li, Q. P., Franks, P. J. S., Landry, M. R., Goericke, R., and Taylor, A. G.: Modeling phytoplankton growth rates and chlorophyll to carbon ratios in California coastal and pelagic ecosystems, J. Geophys. Res. Biogeosciences, 115, 1–12, https://doi.org/10.1029/2009JG001111, 2010.

Marchesiello, P., McWilliams, J. C., and Shchepetkin, A.: Open boundary conditions for long-term integration of regional oceanic models, Ocean Model., 3, 1–20, https://doi.org/10.1016/S1463-5003(00)00013-5, 2001.

Mattern, J. P., Fennel, K., and Dowd, M.: Sensitivity and uncertainty analysis of model hypoxia estimates for the Texas-Louisiana shelf, J. Geophys. Res. Ocean., 118, 1316–1332, https://doi.org/10.1002/jgrc.20130, 2013.

McCarthy, M. J., Carini, S. A., Liu, Z., Ostrom, N. E., and Gardner, W. S.: Oxygen consumption in the water column and sediments of the northern Gulf of Mexico hypoxic zone, Estuar. Coast. Shelf Sci., 123, 46–53, https://doi.org/10.1016/j.ecss.2013.02.019, 2013.

Michaelis, L. and Menten, M. L.: Die kinetik der invertinwirkung, Biochem. Z., 49, 333–369, 1913.

Moriarty, J. M., Harris, C. K., Friedrichs, M. A. M., Fennel, K., and Xu, K.: Impact of Seabed Resuspension on Oxygen and Nitrogen Dynamics in the Northern Gulf of Mexico: A Numerical Modeling Study, J. Geophys. Res. Ocean., 123, 7237–7263, https://doi.org/10.1029/2018JC013950, 2018.

Murrell, M. C. and Lehrter, J. C.: Sediment and Lower Water Column Oxygen Consumption in the Seasonally Hypoxic Region of the Louisiana Continental Shelf, Estuaries and Coasts, 34, 912–924, https://doi.org/10.1007/s12237-010-9351-9, 2011.

Olson, R. J.: Differential photoinhibition of marine nitrifying bacteria: a possible mechanism for the formation of the primary nitrite maximum, J. Mar. Res., 39, 227–238, 1981.

748 Parker, R. A.: Dynamic models for ammonium inhibition of nitrate uptake by phytoplankton, Ecol. Modell., 66, 113–120,
749 https://doi.org/10.1016/0304-3800(93)90042-Q, 1993.

750 Platt, T., Gallegos, C. L., and Harrison, W. G.: Photoinhibition of photosynthesis in natural assemblages of marine phytoplankton, J. Mar.
751 Res., 38, 687–701, 1980.

752 Rabalais, N. N. and Baustian, M. M.: Historical Shifts in Benthic Infaunal Diversity in the Northern Gulf of Mexico since the Appearance
753 of Seasonally Severe Hypoxia, Diversity, 12, https://doi.org/10.3390/d12020049, 2020.

754 Rabalais, N. N. and Turner, R. E.: Gulf of Mexico Hypoxia: Past, Present, and Future, Limnol. Oceanogr. Bull., 28, 117–124,
755 https://doi.org/10.1002/lob.10351, 2019.

756 Rabalais, N. N., Turner, R. E., and Wiseman, W. J.: Gulf of Mexico hypoxia, a.k.a. "The dead zone," Annu. Rev. Ecol. Syst., 33, 235–263,
757 https://doi.org/10.1146/annurev.ecolsys.33.010802.150513, 2002.

758 Rabalais, N. N., Turner, R. E., Sen Gupta, B. K., Boesch, D. F., Chapman, P., and Murrell, M. C.: Hypoxia in the northern Gulf of Mexico:
759 Does the science support the plan to reduce, mitigate, and control hypoxia?, Estuaries and Coasts, 30, 753–772,
760 https://doi.org/10.1007/BF02841332, 2007a.

761 Rabalais, N. N., Turner, R. E., Gupta, B. K. S., Platon, E., and Parsons, M. L.: Sediments tell the history of eutrophication and hypoxia in
762 the northern Gulf of Mexico, Ecol. Appl., 17, 129–143, https://doi.org/10.1890/06-0644.1, 2007b.

763 Rowe, G. T., Cruz Kaegi, M. E., Morse, J. W., Boland, G. S., and Escobar Briones, E. G.: Sediment community metabolism associated with
764 continental shelf hypoxia, northern Gulf of Mexico, Estuaries, 25, 1097–1106, https://doi.org/10.1007/BF02692207, 2002.

765 Saha, S., Moorthi, S., Pan, H.-L., Wu, X., Wang, J., Nadiga, S., Tripp, P., Kistler, R., Woollen, J., Behringer, D., Liu, H., Stokes, D.,
766 Grumbine, R., Gayno, G., Wang, J., Hou, Y.-T., Chuang, H.-Y., Juang, H.-M. H., Sela, J., Iredell, M., Treadon, R., Kleist, D., Van Delst,
767 P., Keyser, D., Derber, J., Ek, M., Meng, J., Wei, H., Yang, R., Lord, S., van den Dool, H., Kumar, A., Wang, W., Long, C., Chelliah, M.,
768 Xue, Y., Huang, B., Schemm, J.-K., Ebisuzaki, W., Lin, R., Xie, P., Chen, M., Zhou, S., Higgins, W., Zou, C.-Z., Liu, Q., Chen, Y., Han,
769 Y., Cucurull, L., Reynolds, R. W., Rutledge, G., and Goldberg, M.: NCEP Climate Forecast System Reanalysis (CFSR) 6-hourly Products,
770 January 1979 to December 2010, https://doi.org/10.5065/D69K487J, 2010.

771 Saha, S., Moorthi, S., Wu, X., Wang, J., Nadiga, S., Tripp, P., Behringer, D., Hou, Y.-T., Chuang, H., Iredell, M., Ek, M., Meng, J., Yang,
772 R., Mendez, M. P., van den Dool, H., Zhang, Q., Wang, W., Chen, M., and Becker, E.: NCEP Climate Forecast System Version 2 (CFSv2)
773 6-hourly Products, https://doi.org/10.5065/D61C1TXF, 2011.

774 Scavia, D., Justić, D., Obenour, D. R., Craig, J. K., and Wang, L.: Hypoxic volume is more responsive than hypoxic area to nutrient load
775 reductions in the northern Gulf of Mexico - And it matters to fish and fisheries, Environ. Res. Lett., 14, https://doi.org/10.1088/1748-
776 9326/aaf938, 2019.

777 Schaeffer, B. A., Kurtz, J. C., and Hein, M. K.: Phytoplankton community composition in nearshore coastal waters of Louisiana, Mar. Pollut.
778 Bull., 64, 1705–1712, https://doi.org/10.1016/j.marpolbul.2012.03.017, 2012.

779 Seitzinger, S. P. and Giblin, A. E.: Estimating denitrification in North Atlantic continental shelf sediments, in: Nitrogen Cycling in the North
780 Atlantic Ocean and its Watersheds, edited by: Howarth, R. W., Springer Dordrecht, 235–260, https://doi.org/10.1007/978-94-009-1776-7_7,
781 1996.

782 Shchepetkin, A. F. and McWilliams, J. C.: The regional oceanic modeling system (ROMS): A split-explicit, free-surface, topography-
783 following-coordinate oceanic model, Ocean Model., 9, 347–404, https://doi.org/10.1016/j.ocemod.2004.08.002, 2005.

784 Shchepetkin, A. F. and McWilliams, J. C.: Correction and commentary for "Ocean forecasting in terrain-following coordinates: Formulation
785 and skill assessment of the regional ocean modeling system" by Haidvogel et al., J. Comp. Phys. 227, pp. 3595-3624, J. Comput. Phys., 228,
786 8985–9000, https://doi.org/10.1016/j.jcp.2009.09.002, 2009.

787 Shropshire, T., Morey, S., Chassignet, E., Bozec, A., Coles, V., Landry, M., Swalethorp, R., Zapfe, G., and Stukel, M.: Quantifying
788 spatiotemporal variability in zooplankton dynamics in the Gulf of Mexico with a physical-biogeochemical model, Biogeosciences, 17, 3385–
789 3407, https://doi.org/10.5194/bg-17-3385-2020, 2020.

790 Simpson, J. H.: The shelf-sea fronts: implications of their existence and behaviour, Philos. Trans. R. Soc. London. Ser. A, Math. Phys. Sci.,
791 302, 531–546, https://doi.org/10.1098/rsta.1981.0181, 1981.

792 Simpson, J. H. and Bowers, D.: Models of stratification and frontal movement in shelf seas, Deep Sea Res. Part A, Oceanogr. Res. Pap., 28,
793 727–738, https://doi.org/10.1016/0198-0149(81)90132-1, 1981.

794 Simpson, J. H. and Hunter, J. R.: Fronts in the Irish Sea, Nature, 250, 404–406, https://doi.org/10.1038/250404a0, 1974.

795 Simpson, J. H., Allen, C. M., and Morris, N. C. G.: Fronts on the Continental Shelf, J. Geophys. Res., 83, 4607–4614,
796 https://doi.org/10.1029/JC083iC09p04607, 1978.

797 Tao, B., Tian, H., Ren, W., Yang, J., Yang, Q., He, R., Cai, W., and Lohrenz, S.: Increasing Mississippi river discharge throughout the 21st
798 century influenced by changes in climate, land use, and atmospheric CO2, Geophys. Res. Lett., 41, 4978–4986,
799 https://doi.org/10.1002/2014GL060361, 2014.

800 Wang, L. and Justić, D.: A modeling study of the physical processes affecting the development of seasonal hypoxia over the inner Louisiana-
801 Texas shelf: Circulation and stratification, Cont. Shelf Res., 29, 1464–1476, https://doi.org/10.1016/j.csr.2009.03.014, 2009.

802 Wanninkhof, R.: Relationship Between Wind Speed and Gas Exchange Over the Ocean, J. Geophys. Res., 97, 7373–7382,
803 https://doi.org/10.1029/92JC00188, 1992.

804 Warner, J. C., Geyer, W. R., and Lerczak, J. A.: Numerical modeling of an estuary: A comprehensive skill assessment, J. Geophys. Res. C
805 Ocean., 110, 1–13, https://doi.org/10.1029/2004JC002691, 2005.

806 Warner, J. C., Armstrong, B., He, R., and Zambon, J. B.: Development of a Coupled Ocean-Atmosphere-Wave-Sediment Transport
807 (COAWST) Modeling System, Ocean Model., 35, 230–244, https://doi.org/10.1016/j.ocemod.2010.07.010, 2010.

808 Warner, J. C., Defne, Z., Haas, K., and Arango, H. G.: A wetting and drying scheme for ROMS, Comput. Geosci., 58, 54–61,
809 https://doi.org/10.1016/j.cageo.2013.05.004, 2013.

810 Wawrik, B. and Paul, J. H.: Phytoplankton community structure and productivity along the axis of the Mississippi River plume in
811 oligotrophic Gulf of Mexico waters, Aquat. Microb. Ecol., 35, 185–196, https://doi.org/10.3354/ame035185, 2004.

812 Yu, L., Fennel, K., and Laurent, A.: A modeling study of physical controls on hypoxia generation in the northern Gulf of Mexico, J. Geophys.
813 Res. Ocean., 120, 5019–5039, https://doi.org/10.1002/ 2014JC010634, 2015.

814 Zang, Z., Xue, Z. G., Bao, S., Chen, Q., Walker, N. D., Haag, A. S., Ge, Q., and Yao, Z.: Numerical study of sediment dynamics during
815 hurricane Gustav, Ocean Model., 126, 29–42, https://doi.org/10.1016/j.ocemod.2018.04.002, 2018.

816 Zang, Z., Xue, Z. G., Xu, K., Bentley, S. J., Chen, Q., D'Sa, E. J., and Ge, Q.: A Two Decadal (1993–2012) Numerical Assessment of
817 Sediment Dynamics in the Northern Gulf of Mexico, Water, 11, 938, https://doi.org/10.3390/w11050938, 2019.

818 Zang, Z., Xue, Z. G., Xu, K., Ozdemir, C. E., Chen, Q., Bentley, S. J., and Sahin, C.: A Numerical Investigation of Wave-Supported Gravity
819 Flow During Cold Fronts Over the Atchafalaya Shelf, J. Geophys. Res. Ocean., 125, 1–24, https://doi.org/10.1029/2019JC015269, 2020.